UC Riverside
UC Riverside Electronic Theses and Dissertations

Title

Ultra-High Resolution 1S-2S Spectroscopy of Positronium

Permalink

https://escholarship.org/uc/item/85n6z7ps

Author

Liu, Yuanqian

Publication Date

2021

Peer reviewed|Thesis/dissertation

UNIVERSITY OF CALIFORNIA
RIVERSIDE

Ultra-High Resolution 1^3S_1-2^3S_1 Spectroscopy of Positronium

A Dissertation submitted in partial satisfaction
of the requirements for the degree of

Doctor of Philosophy

in

Physics

by

Yuanqian Liu

December 2021

Dissertation Committee:
    Dr. Harry W. K. Tom, Chairperson
    Dr. Allen P. Mills, Jr.
    Dr. Hai-bo Yu

The Dissertation of Yuanqian Liu is approved:

_____

_____

_____
Committee Chairperson

University of California, Riverside

Acknowledgments

Foremost, I would like to express my sincere gratitude to my advisor, Prof. Harry Tom, who offered me this great opportunity to participate in such an exciting scientific program. His enthusiasm for physics and the constant pursuit of truth is contagious and always motivate me. His profound knowledge and experience are enlightening. And his optimism has been encouraging through the crest and troughs of this academic journey.

I would also like to thank Prof. Allen Mills, who constantly shows up in the lab and cast insightful and creative ideas upon the experiments. Many of the achievements could not have been accomplished without his suggestions. And without his tireless effort in the realm of positron and positronium physics, this experiment would not be possible.

I appreciate the help from Harris Goldman, who laid the foundation of the apparatus of this experiment with his tremendous effort. He offered me helpful instructions and led me into this project. His patient guidance helped me quickly pick up the details and start to work independently. His diligence and work ethic also set a role model for me. I am grateful for his advice in both the academic field and personal life.

Thanks to all my colleagues for their excellent work on the positron beamline. I am grateful for the generous help and the brilliant ideas they shared.

An important thank you to the machine shop for all the machining work they have done for us and the machining skills they tutored me.

Last but not least, I would like to thank my family for your unconditional love and support throughout my life. I could not have made it through this journey without you. My gratitude to you is inexpressible. Thank you!

ABSTRACT OF THE DISSERTATION

Ultra-High Resolution 1^3S_1-2^3S_1 Spectroscopy of Positronium

by

Yuanqian Liu

Doctor of Philosophy, Graduate Program in Physics
University of California, Riverside, December 2021
Dr. Harry W. K. Tom, Chairperson

Positronium (Ps) is an exotic hydrogen-like atom consisting of an electron and its antiparticle—positron. As a pure leptonic atom, positronium is a perfect source to test quantum electrodynamics (QED). The leptonic hydrogen-like structure also makes it an ideal test bench for the proton radius puzzle—the discrepancy in the measurement of proton charge radius using different methods and atoms. Recently, hydrogen spectroscopy has been conducted to relative uncertainties of 10^{-15}. Benefitting from the unique structure of Ps atoms, Ps spectroscopy only needs a precision three orders of magnitude lower for the same level of impact. However, the path to this target is still full of challenges. Due to annihilation, Ps's lifetime is relatively short. The limited lifetime of Ps significantly increased the challenge for Ps spectroscopy. Excitation of Ps atoms into Rydberg states can effectively extend the lifetime of Ps atoms for detection. However,

many other challenges exist, such as the uncertainty in the energy level induced by its transient lifetime.

The last positronium 1^3S_1-2^3S_1 spectroscopy was performed by Fee, Mills, Chu, et al. almost thirty years ago. It reached a relative uncertainty of 3.2 ppb, and the measured 1^3S_1-2^3S_1 interval was 1.7σ away from the theoretical calculation. In 2020, Gurungs et al. measured the Ps n=2 fine structure and also found a disagreement with the theoretical value.

This paper presents the development of the instrument we built for positronium precision spectroscopy and our current experiments. The apparatus includes an ultrahigh finesse optical interferometer for positronium two-photon excitation, a frequency stabilizing system, a frequency comb for ultra-precise spectroscopy, and pulsed lasers for $2P/2S$ to Rydberg excitation. We have achieved a positronium $1S$-$2P$ excitation with a 7× improvement in yield compared with the last experiment in 2018. Ps 1^3S_1-2^3S_1 spectroscopy experiments are under operation, and we expect a 10-1000 improvement in precision from the previous experiment.

Contents

List of Figures

List of Tables

Chapter 1

Introduction

1.1 Positronium

1.1.1 History of positron and positronium

In 1928, Paul Dirac published the famous Dirac equation, which successfully unified quantum mechanics and special relativity [1]. One achievement of the Dirac equations is a prediction of the existence of both positive and negative energy levels of an electron. One year later, Dirac made an attempt to explain the negative-energy solutions of his equation to be a particle that behaves as if it has a positive charge [2] and discussed the possibility that this solution indicates a proton. Robert Oppenheimer convinced Dirac of the impossibility of the "proton" conjecture by showing him the induced rapid destruction of a hydrogen atom. In 1931, Dirac claimed that this negative-energy electron should be an antiparticle—positron [3]. One year later, positrons were first observed experimentally by Carl David Anderson [4], which won him the 1936 Nobel Prize in Physics.

A hydrogen-like atom consisting of an electron and a positron was predicted by Stjepan Mohorovičić in 1934 [5]. Seventeen years later, this exotic atom was experimentally observed in MIT by Deutsch, and it was named positronium (Ps) [6]. Since the first demonstration of it, Ps has undergone extensive study. Thirty-two years

later, the first two-photon excitation of Ps was first realized by Chu and Mills in 1983 [7]. Molecules formed by Ps atoms were also predicted [8] and observed. Observation of di-positronium molecules was published by Cassidy and Mills in 2007 [9].

1.1.2 Physics of Ps Atoms

Ps is an exotic hydrogen-like atom formed by an electron and a positron. Since it is a bounded state of a particle and its antiparticle, the electron and the positron comprising the atom eventually annihilate with the emission of gamma-photons (γ). The decaying process of a Ps atom can take two distinct processes depending on its atomic structure—a direct self-annihilation or a radiative decay followed by self-annihilation at lower energy levels [10].

The lifetime of a Ps atom depends on its principal, angular quantum numbers, as well as spin polarization because these factors determine what decay process a Ps will take. The self-annihilation contribution to the decaying process predominantly depends on the overlap of the electron and positron wave functions. It scales with the cube of the principal quantum number n^3. Also, when the angular quantum number $l > 0$, the overlap is practically zero [11]. Under such circumstances, although two-photon and three-photon processes can still contribute to Ps annihilation, the rate of these processes is negligible experimentally [12, 13]. Consequently, the radiative process dominates the lifetime of a high-order (n > 1) state Ps.

One exception is the $2S$ state Ps. As hydrogen and helium [14], a $2S$ state Ps is metastable, as the selection rule forbids a $2S$ Ps from decaying into a $1S$ state by single-photon emission. Thus the dominant contribution to the decaying of $1S$ or $2S$ Ps states is

direct self-annihilation. However, the lifetimes of singlet and triplet states of Ps are significantly different since the spin polarizations strongly affect the orbital wave function overlapping of Ps particles.

For example, 1^1S_0 Ps possesses an annihilation lifetime of approximately 124 ps in vacuum [15], while its triplet counterpart, 1^3S_1 Ps, has a lifetime more than a thousand times longer at 142ns [16]. In contrast, a 2^1S_0 Ps can exist for about 1ns while the 2^3S_1 Ps lifetime is 1.1μs [17]. As is indicated in Fig. 1.1 [18], the lifetime of a $2P$ Ps is dominated by the Lyman-α emission at 3.2 ns rather than annihilation. The 1.1μs lifetime of 2^3S_1 Ps is already long enough to allow a portion of Ps to reach the detector. However, excitation into higher states could effectively extend the lifetime of Ps atoms, which can facilitate the detection of Ps atoms when a long flying trajectory is necessary.
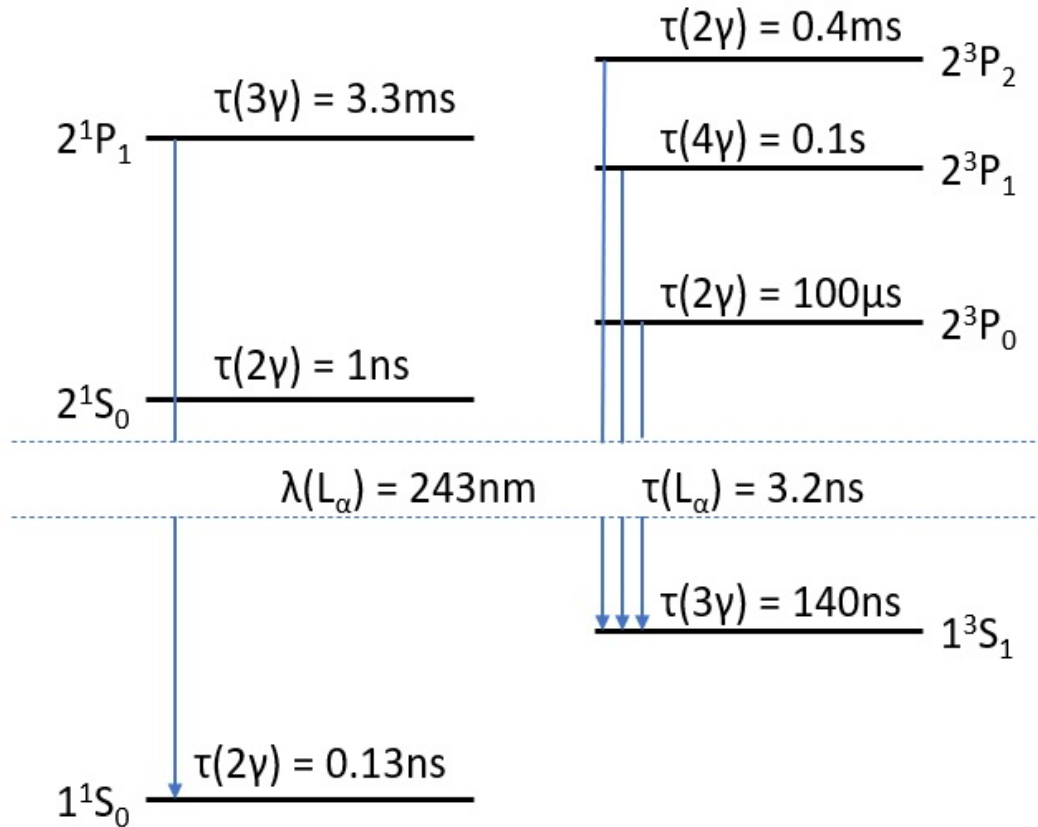
Figure 1.1: Annihilation and Lyman-α emission lifetimes of 2P state positroniums.

Despite its transient lifetime, Ps possesses many incomparable advantages. Unlike hydrogen or other atoms with nuclear structure, Ps is purely leptonic and free from nuclear effects. The small masses of electron and positron make the weak force contribution to Ps energy levels negligible [19, 20]. As a result, Ps energy levels can be described by QED with extreme precision. However, discrepancies have emerged

between experiment and theory by a recent work of Gurung, Babij, Hogan, and Cassidy [21].

Ps also provides a test bench for the proton charge radius puzzle, where discrepancies occurred in the measurements of the proton charge radius of hydrogen atoms and muonic hydrogen atoms. The pure leptonic Ps will test the possibility of contributions to this discrepancy from nuclear structures. Further discussion regarding this puzzle will be shown in section 1.2.

Ps atoms also possess an advantage over other leptonic atoms, such as muonium, owing to its unique mass ratio $m/M = 1$. The radiative-recoil correction $\alpha(Z\alpha)^6(m^3/M^2)$ or the pure recoil correction $(Z\alpha)^7(m^3/M^2)$ can be tested two orders of magnitude higher in precision compared with using muonium as the source, where $m/M \approx 1/200$. However, annihilation terms must be included in high-order corrections.

In theoretical calculation, the Ps energy levels are expanded into terms in the form of $m_e\alpha^n(ln\ \alpha)^m$ or $R_\infty\alpha^{n-2}(ln\ \alpha)^m$, with R_∞ being the Rydberg constant that equals $\alpha^2 m_e c/2h$, α being the fine structure constant, m_e being the electron mass, c being the speed of light, and h being the Planck constant. Equation 1.1 [22] presented a list of correction terms that have been calculated:

$$\frac{E_0}{h} = -\frac{1}{2n^2}c(R_\infty)$$

$$\frac{E_1}{h} = 2\frac{1}{n^3}c(R_\infty\alpha^2)\left[\frac{11}{64}\frac{1}{n} + \frac{1}{12}\right]$$

$$\frac{E_2}{h} = -\frac{6}{4\pi}\frac{1}{n^3}c(R_\infty\alpha^3 ln\alpha)$$

$$\frac{E_3}{h} = \frac{1}{4\pi}\frac{1}{n^3}c(R_\infty\alpha^3)\left\{\frac{14}{3}\left[\frac{7}{15} + \ln\left(\frac{2}{n}\right) + \frac{n-1}{2n} + \sum_{k=1}^{n}\frac{1}{k} + ln2\right] - \frac{16}{3}lnR(n,0) - 4\left(\frac{16}{9} + ln2\right)\right\}$$

$$\frac{E_4}{h} = -\frac{1}{6}\frac{1}{n^3}c(R_\infty\alpha^4 ln\alpha)$$

$$\frac{E_5}{h} = \begin{cases} 2c(R_\infty\alpha^4)\left[0.16107(63) + 0.3925(17)\times\frac{1}{4}\right], & n = 1 \\ \frac{1}{4}c(R_\infty\alpha^4)\left[0.34557(63) - 0.1048(17)\times\frac{1}{4}\right], & n = 2 \end{cases}$$

$$\frac{E_6}{h} = -\frac{2}{\pi}\frac{1}{n^3}c(R_\infty\alpha^5 ln^2\alpha)\frac{151}{120}$$

Equation 1.1

So far, all correction terms on the scale of $O(R_\infty\alpha^4)$ have been calculated [23-28], and many $O(R_\infty\alpha^5)$ corrections have been reported [29-35], but a thorough calculation on this order is not finished. A review of $O(R_\infty\alpha^5)$ corrections can be found in [36]. The contributions from $O(R_\infty\alpha^4)$ are on the MHz scale, while the $O(R_\infty\alpha^5)$ corrections are down to kHz.

In 2018 CODATA suggested values [37], many constants appearing in the equations above have evolved from those of 2014 CODATA [38]. The Planck constant is defined to an exact value of $6.626\,070\,15\times10^{-34}$ as a definition of kilogram in SI units, as opposed to the previous experimental value at $6.626\,070\,040(81)\times10^{-34}$. The Rydberg

constant R_∞ and fine-structure constant α are re-defined to 10 973 731.568 160(21) m^{-1} and 7.297 352 5693(11) × 10^{-3} respectively from previous values at 10 973 731.568 508(65) m^{-1} and 7.297 352 5664(11) × 10^{-3}. These corrections result from analyzing the covariance between the uncertainties of proton charge radius (r_p) and R_∞, and adjusting the r_p and R_∞ values to achieve an error covariance ellipse with a rounder shape.

Experimentally, the most recent measurement of Ps 1^3S_1-2^3S_1 interval was demonstrated by Fee et al. [39] in 1993 with a result of $\Delta E(1^3S_1 - 2^3S_1) = 1\,233\,607\,216.4(3.2)$ MHz, which is about 1.7σ different from the theory. Moreover, a recent measurement of Ps n=2 fine structure by Gurung et al. [21] demonstrated a difference from the theoretical calculation by 4.5σ.

The results of these measurements urge further progress in Ps spectroscopy. Experimental measurements with kHz scale precision and a complete calculation of $O(R_\infty \alpha^5)$ terms will facilitate tests of QED theory and provide another approach for precision measurement R_∞, which hopefully can draw a conclusion to the proton radius puzzle.

1.2   Proton Charge Radius Puzzle

The proton charge radius (r_p) puzzle is an unsolved problem aroused by discrepancies in measurements of proton charge radius from different experiments. Measurements of proton charge radius were mainly performed through two approaches, electron-proton (e-p) scattering and hydrogen spectroscopy. Before 2010, the values 0.8768(69)fm [40] from hydrogen and 0.8775(51)fm from e-p scattering [41]) agreed with each other.

However, Pohl et al. [42] performed spectroscopy of the Lamb shift on the $n = 2$ level of muonic hydrogen atoms (μ-H), which comprises a negative muon and a proton, and achieved an $r_p = 0.842(1)$fm, a value 5σ below the previous reports. Another μ-H $n = 2$ level spectroscopy was conducted by Antognini et al. [43] in 2013 with an r_p value agreeing with Pohl's measurement but distinct from pre-2010 results.

Since Pohl, more experiments have been conducted to measure r_p, and different results have shown up. Even with similar experimental approaches, different r_p values emerged. Some works are shown below.

With the spectroscopy approach, Beyer et al. achieved an $r_p = 0.8335(95)$fm by the $2S$-$4P$ transition of atomic hydrogen in 2014 [44], while Fleurbaey et al. estimated an $r_p = 0.877(13)$fm by the $1S$-$3S$ spectroscopy of hydrogen atoms in 2018 [45]. One year later, Bezginov et al. reported an approach less dependent on the Rydberg constant utilizing the $n = 2$ Lamb shift of hydrogen atoms, and r_p was estimated to be 0.833(10)fm.

The e-p scattering approaches also have different results reported. In 2019, Xiong et al. measured an $r_p = 0.831(7)$fm [46], while Mihovilovič acquired a much larger value at 0.870(28)fm [47]. The most recent work in the measurement of r_p is from Hayward et al. in 2020, with a value very close to Pohl's data at 0.842(4)fm [48]. Fig 1.2 shows a comparison of these measured radii and their uncertainties.
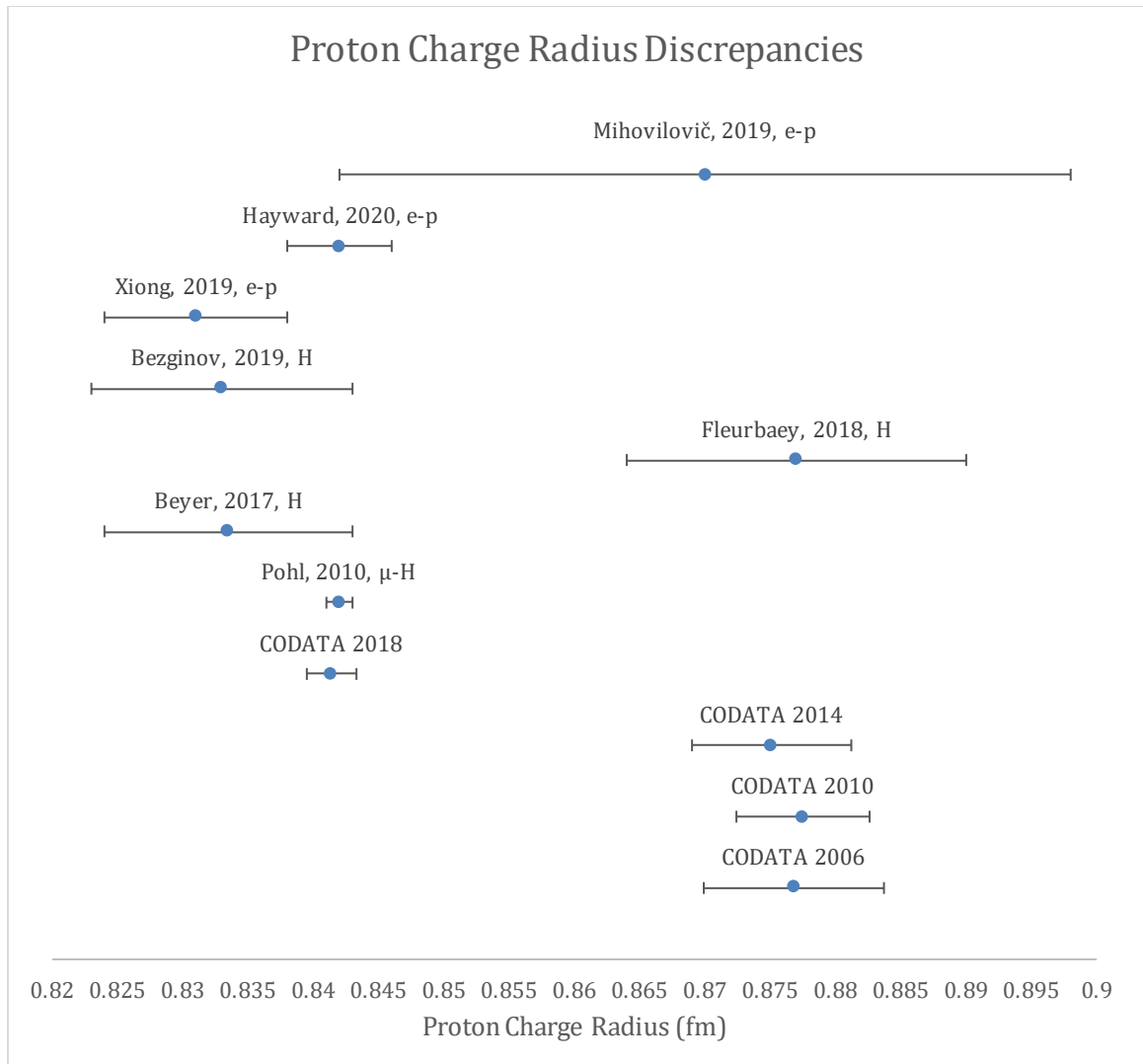
Figure 1.2 Discrepancies in the measurement of proton charge radius.

As is shown in Fig 1.2, r_p values cluster into two categories, a small value where $r_p \approx 0.84$fm and a large one where $r_p \approx 0.88$fm. Many possibilities and novel theories have been proposed for an explanation of this discrepancy [49-51]. A partial solution based on the correlation between r_p and R_∞ has been explored in the 2018 CODATA [37]. A strong covariance error ellipse between the measured r_p and R_∞ was demonstrated in this paper, and corrections have been made to mitigate this correlation. Consequently, the

suggested value of r_p from the 2018 CODATA was corrected to a smaller value with a simultaneous correction on R_∞.

However, this partial solution in 2018 CODATA is based simply on the pursuit of a rounder covariance error ellipse and did not bring a conclusion. As pure QED atoms, Ps spectroscopy with kHz precision could provide another approach to resolve this problem. Ps 1^3S_1-2^3S_1 precision spectroscopy can give a Rydberg constant within the framework of QED and a correlated r_p value. However, we are looking forward to more Ps spectroscopy experiments to bring a conclusion to R_∞ measurement. If discrepancies still occur in measured R_∞ values, the effectiveness of QED theory needs to be discussed, and new physics may be discovered.

1.3 Review of the Progress in Ps Spectroscopy

Most of the Ps spectroscopy experiments are more than 25 years old. In these experiments, Ps $n = 1$ hyperfine structure and $n = 2$ fine structure were reported [52-59]. The Ps interval of our interest—1^3S_1-2^3S_1 interval, was last measured by Fee et al. in 1993 [39]. The error bar of the previous measurement was 3.2 MHz or 2.6 ppb, 1.7σ away from the theoretical calculation. However, due to the relatively large error bar, no assertion could be made regarding this difference.

Recently, work from Gurung et al. demonstrated some exciting results [21, 60]. Gurung et al. measured the n =2 fine structure of Ps, and the υ_0 transition at 18501.02(61) MHz demonstrated a 4.5σ disagreement from the theoretical value of 18498.25(8) MHz. However, further calculation on the kHz scale correction terms and more Ps spectroscopy

experiments are required to explore the physics in this 4.5σ disagreement that Gurung et al. reported.

The following part of this paper will demonstrate the progress of the ultra-precise Ps 1^3S_1-2^3S_1 spectroscopy based on the previous work of Harris Goldman [22]. The ultimate goal is to achieve kHz scale precision measurement of Ps 1^3S_1-2^3S_1 interval, which hopefully can facilitate the testing of QED theory and bring a conclusion to the proton charge radius puzzle.

Chapter 2

Positron Beamline

2.1   Overview

A positron beamline is used to generate, bunch, accelerate, and focus positron pulses. The positron pulse is implanted into a sample target residing in the ultrahigh vacuum chamber where the high-power optical interferometer is located. After the positron injection, Ps atoms re-emitted from the sample will fly through the excitation region towards the multiple-channel detector and be detected if excited to the desired states. This chapter overviews the positron beamline, which can be segmented into four stages: e^+ source, trapping stage, positron optics, and Ps generation stage.

2.2   Positron Source

A widely used method to generate slow positrons favorable for experiments is through the β^+ decay process of radioactive materials. β^+ decay is a process in which a proton in an atom nucleus turns into a neutron with the emission of a positron, an electron neutrino, and a γ-photon:

$$p \rightarrow n + e^+ + v_e + \gamma$$
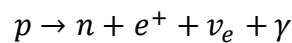
Equation 2.1

The β^+ decay process can be found in many isotopes such as [48]V, ^{64}Cu, ^{68}Ga, or [126]I. We choose [22]Na as our source due to its relatively long lifetime of 2.6 years and high yield positron generation [61]. The β^+ decay for [22]Na is shown in the equation below:

$$^{22}_{11}Na \rightarrow {}^{22}_{10}Ne + e^+ + v_e + \gamma \; (1.27 MeV)$$
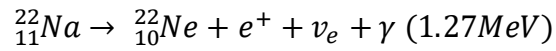
Equation 2.2

The radioactivity of the [22]Na source, which was installed in November 2019 at 50mCi, is currently at 30mCi by August 2021. The source is typically renewed every five years.

The e^+ directly emitted from the source possesses energy up to half of MeV, which is undesirable for the following stages. A moderator and a slow positron selection mechanism are necessary. A schematic of these parts in the source stage is shown in Fig. 2.1.
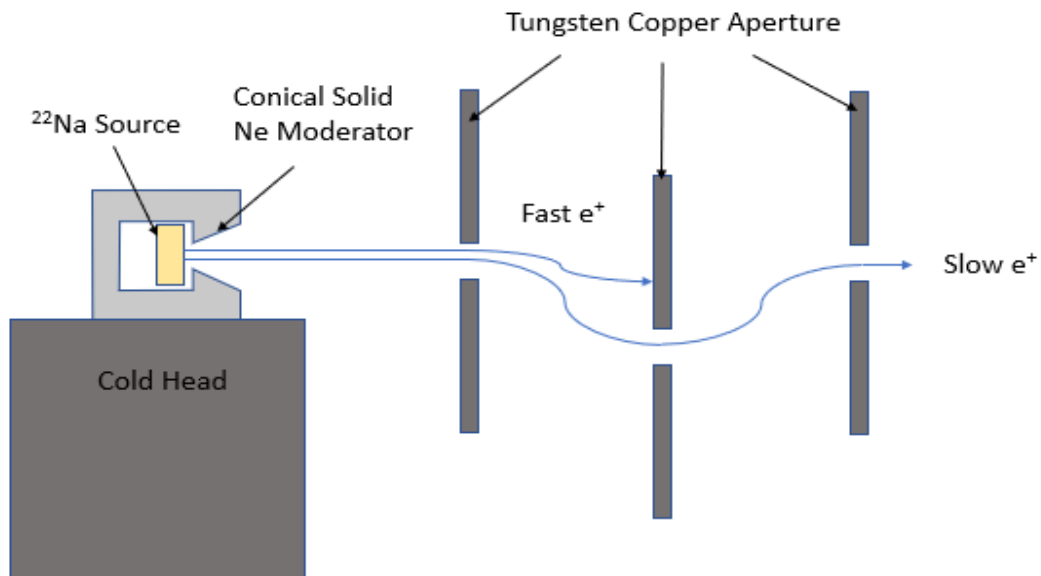
Figure 2.1 Schematic of positron source stage moderator and velocity selector

Neon gas is leaked into the chamber and deposits on the 7K cone structure next to the sodium sample. The solid Neon acts as a moderator [62, 63], and the moderated e^+ energy drops down to several eV. Other noble gas or metal could be used as moderators, but Neon is chosen as it provides the best-known efficiency at 0.4%.

The fast and slow positrons then enter the subsequent area, where a magnetic field diverts their trajectory. Fast positron with smaller diversion of trajectory will eventually hit on the frame of the tungsten-cooper alloy aperture and annihilate. In contrast, slower ones will go through all the apertures and enter the next stage. Solenoids are used to generate another magnetic field along the beamline to limit the trajectory of e^+ radially, preventing them from hitting the wall and ending up in annihilation.

2.3   Trapping

The positrons leaving the source stage will enter a trapping system first introduced by Surko et al. [64-67]. Fig. 2.2 shows a schematic view of the Surko trap. Nitrogen gas and SF_6 gas are leaked into the center tube and the chamber, respectively, and there is no sealing between the tube and the chamber. In each segment, Positrons experience inelastic collisions with N_2 and SF_6 particles, transferring about 9eV of their kinetic energy to the vibrational modes, rotational modes, and electronic excitations of N_2 [68] and SF_6 [69] molecules. In the last segment, positrons are trapped into the potential well formed by the electrodes and eventually reach a thermal equilibrium through repeated collisions with gas particles.
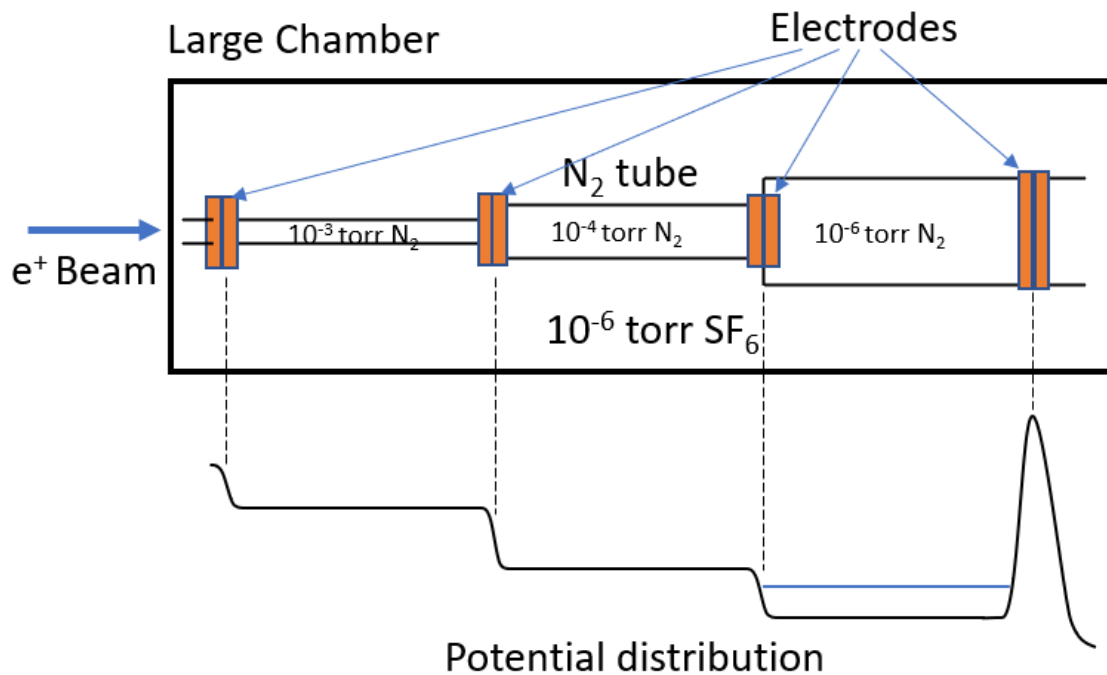
Figure 2.2 Schematic of a Surko trap for positron

The N_2 and SF_6 pressure in each stage is selected so that positrons can lose their kinetic energy effectively yet not annihilate too fast with the electrons in these gas atoms. Different gas pressures are achieved by enlarged diameters of the center tube from one segment to the next.

A solenoid is wrapped around the chamber's outer wall, providing an axial magnetic field that forces positrons into cyclotron motion, thus confining the radial distribution of the positron atoms. However, collisions between positrons and gas molecules may disturb the cyclotron motion and expand the radial distribution of the trapped positrons. A segmented set of electrodes can apply a rotating potential at the frequency of 5.3 MHz producing a compressing effect on the positron cloud that

counteracts the diffusion. The extra energy induced by this rotating potential dissipates quickly through the interaction with gas particles.

The number of trapped positrons depends on the radioactivity of the source and the trapping frequency. The 5 mCi ^{22}Na source before November 2019 can produce approximately 10^5 trapped positrons every 500 ms. A new 50 mCi ^{22}Na source was installed in November 2019. In August 2021, the source's radioactivity is 30 mCi, and about 3×10^5 positrons can be trapped every 500 ms.

Due to the leaking of N_2 and SF_6, the trapping stage must be "isolated" from the former and latter ultrahigh vacuum stages of the beamline. Differential pumping is used for the "isolation." The connection between each end of the trap to the neighboring stage is by a 4 ft long and 1/10 inch wide tube, with a turbopump attached in the middle to suck out the residual gas. The diffusion rate scales with the square of the diameters. Thus with differential pumping, an adjacent stage can have a 10^{-9} torr vacuum, three orders lower than the trapping system.

2.4 Accelerator and Positron Optics

Following the trap are the accelerator and positron optics. One approach we are adopting to improve the precision from Fee [39] is to record the information for each excited Ps particle individually, including the transition frequency and the trajectory information. Good temporal and spatial resolutions of e^+ trajectory are significant in the calculation of correction terms. Positron optics focuses the e^+ pulse onto a small spot (0.3mm) on the sample, providing an excellent resolution on the starting end of the Ps trajectories. Fig. 2.3 shows a side view of this stage.
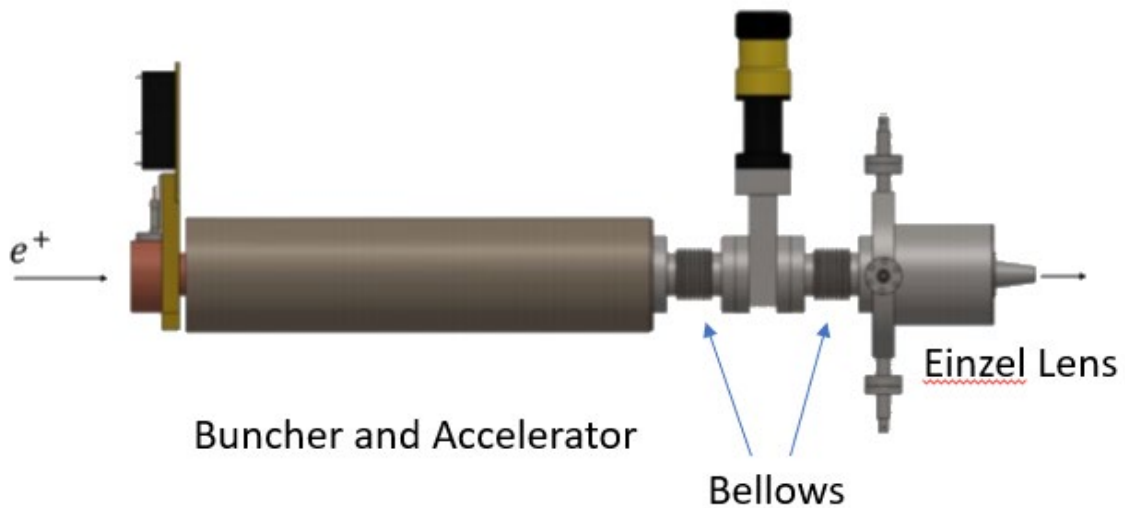
Figure 2.3 Positron optics

This stage has two segments — the buncher accelerator and the electrostatic lens (Einzel lens), with a gate valve and two welded bellows in the middle. The gate valve is mounted directly to the ground by a 4'×12' stainless steel tower. This connection is designed to prevent the mechanical vibrations generated from the former part of the e^+ beamline from transmitting onto the Einzel lens, which is attached to the optical cavity vacuum chamber.

The buncher and accelerator are enveloped in a μ-metal shield. The first one-third of this segment has a parabolic field that can compress the 30 ns positron pulse out of the trapping stage to < 10 ns. The following two-thirds is an accelerator with a linear potential that propels positrons adiabatically up to several keV, which conserves the positron pulse's phase distribution. A tunable final velocity with a 200eV FWHM energy spread could be achieved. This segment terminates with a μ-metal aperture preventing the

magnetic field from leaking into the optical chamber, which can cause undesirable Zeeman shift in Ps 1S-2S transition.

The Einzel lens, as shown in Fig. 2.4, consists of three cylindrical electrodes, the first and last of which are grounded while a non-zero voltage is applied to the middle one. The positron beam passing through this field will be focused on a 0.3 mm spot on the sample target.

To avoid electric field leakage and the Stark Shift it induces. The tapered nozzle of the Einzel lens is grounded and mounted at >10cm distance from the Ps excitation region.
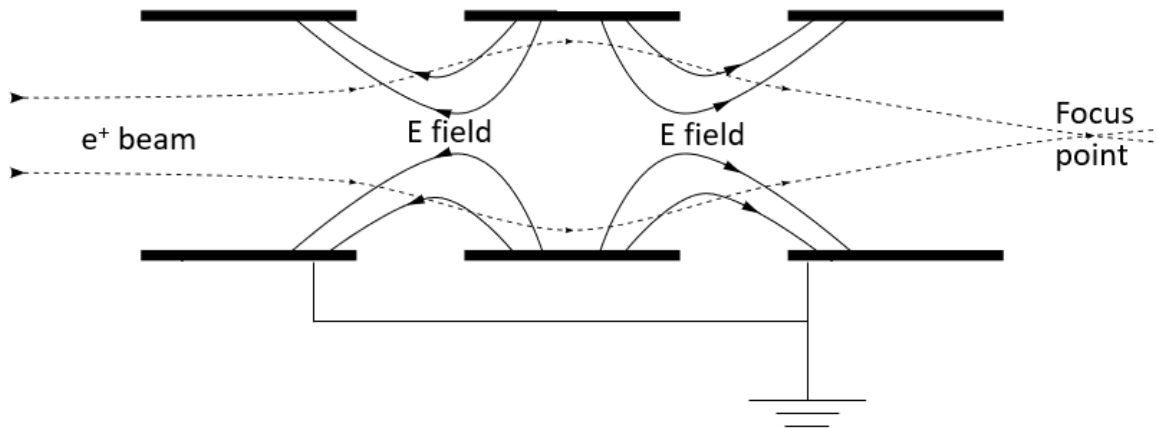
Figure 2.4 Positron path focused by Einzel lens

2.5   Ps Generation on Sample

The Einzel lens is tuned such that the slow positron beam is focused onto a sample mounted near the optical axis of the interferometer. When slow positrons are injected into the sample, they could annihilate with the electrons, be re-emitted at lower

velocities [70], or be emitted in bound states with electrons as Ps. The Ps can be emitted with a thermal energy distribution [71-73] or a monoenergetic distribution [74].

The yield of Ps atoms depends on the implantation depth, the temperature of the sample, and the material selection of the sample [75, 76]. The sample could be monocrystalline metals such as aluminum or copper, or porous silica, depending on the design of the experiment.

For example, implanting e^+ into a single-crystal aluminum target's (111) surface could generate sub-room-temperature slow Ps with 1-2 eV energy [77] that is favorable for our experiment. However, aluminum is easily oxidized or contaminated, resulting in a significant drop in the yield of Ps. Restoring cleanness requires processes such as Ar^+ bombardment or annealing.

Porous silica is more resilient from contamination and can generate thermalized Ps at 300K. Unfortunately, Ps atoms could spend a delay time inside the porous material up to 30ns [78]. The trajectory length of an excited Ps atom is about 30cm, and the velocity is around 1×10^5m/s. So 30ns delay time may lead to 1~2% uncertainty when calculating the time of flight (ToF) of each Ps atom.

Due to the consideration above, we are currently performing Ps 1S-2S and 1S-2P excitation with a porous silica target and will switch to Al in future experiments. To reduce the uncertainty induced by the delay time, we seek slow positrons with longer ToF.

The Ps generated from the target comprise mostly ground-state atoms and a small amount of excited-state atoms [79]. In ground-state atoms, three-quarters are triplet states, which we prefer in our experiment.

The triplet Ps are subsequently single-photon excited by a 243 nm pulsed dye laser to 2P states or two-photon excited by a 486nm CW laser to a 2S state. However, neither of these states has long enough a lifetime to reach the detector efficiently, which is 30cm away from the sample. The most probable velocity for thermalized Ps from a porous silica target is 1×10^5m/s, so the 30cm path length requires about 3000ns ToF. This most probable ToF is much larger than the 3.2ns lifetime of 2P triplet states and is comparable to the 1.1μs lifetime of the 1S triplet state. ToFs for slow positrons, which we are most interested in, are even longer than 3000ns.

The problem can be solved by exciting $n = 2$ Ps atoms to Rydberg states, where n = 20 ~ 30, by a pulsed IR dye laser. The wavelength of the dye laser is tunable between 731 nm – 735 nm, depending on to which states the Ps atoms are excited. The wavelength difference between different yielding peaks can be used to identify the n of the excited state.

As discussed in 1.1.2, the lifetime of a Rydberg Ps is dominated by radiative decay, and the lifetime can be affected by the principal, azimuthal, and magnetic quantum numbers [80]. For an $n = 20$ Rydberg state, the lifetime is prolonged to 30 μs, and the decaying loss is reduced to less than 10%.

Although all Rydberg states with n>20 have a long lifetime, we use a moderate n number of 20~30 instead of, for example, n=100 because high Rydberg state Ps atoms tend to be ionized in front of the MCP detector. The free-electron from ionized Ps can be displaced by the field of MCP, which may not be perfectly vertical, and affect the landing position measurement or the trajectory of Ps atoms.

2.6   Ps Count Rate

The positrons generated from the currently 30mCi source are moderated by solid Neon with 0.04% efficiency, and slow positrons are collected and trapped in the buffer gas trap with up to 20% efficiency. Nearly all the Ps atoms ($\sim10^5$) in the trapping stage can be accelerated and focused by the buncher accelerator. Among all e^+ atoms, about 1/3 annihilate in the target, 1/3 are ejected as e^+, and 1/3 are ejected as Ps. However, only thermal Ps atoms at the triplet ground state are helpful for our experiment. By analyzing the Gamma-radiation signal, we find that 6%~15% of the e^+ particles turn into delayed Ps atoms, which means their Gamma-ray radiation exhibits lifetimes of about 142ns. We estimate that 7000 1S thermal Ps atoms could be ejected from the sample. Their trajectories distribute evenly into the 2π solid angle on top of the sample surface. The MCP plate has a 3" diameter and is located about 30cm away. By calculating the percentage of the solid angle, only 1.6% of the 7000 Ps, or 110 atoms, are flying towards the MCP. Our experiment needs to use these atoms and excite them to the target states.

Chapter 3

Optical Spectroscopy Apparatus

3.1   Overview of Apparatus
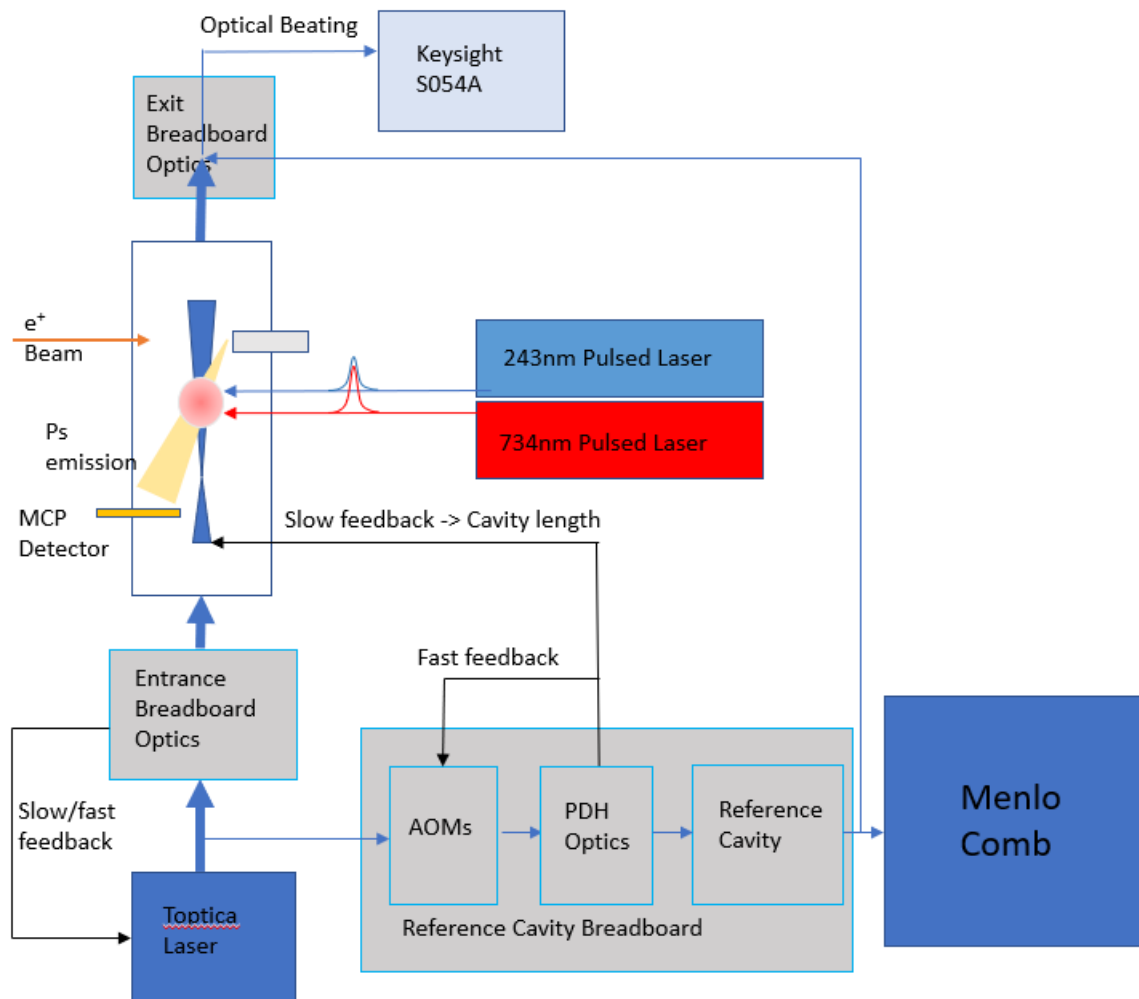
Figure 3.1 Schematic overview of the optical spectroscopy apparatus

A schematic overview of the optical spectroscopy apparatus is demonstrated in Fig 3.1. It can be divided into four sections: the ultrahigh vacuum (UHV) spectroscopy chamber, the reference cavity breadboard, the frequency comb, and pulsed lasers. These four regions are spacially separated yet connected through optical or electrical circuits. Blue arrows demonstrate the flow of optical signals with their thickness qualitatively indicating the intensity of the laser beam, and the black arrows indicate the flow of electric feedback signals.
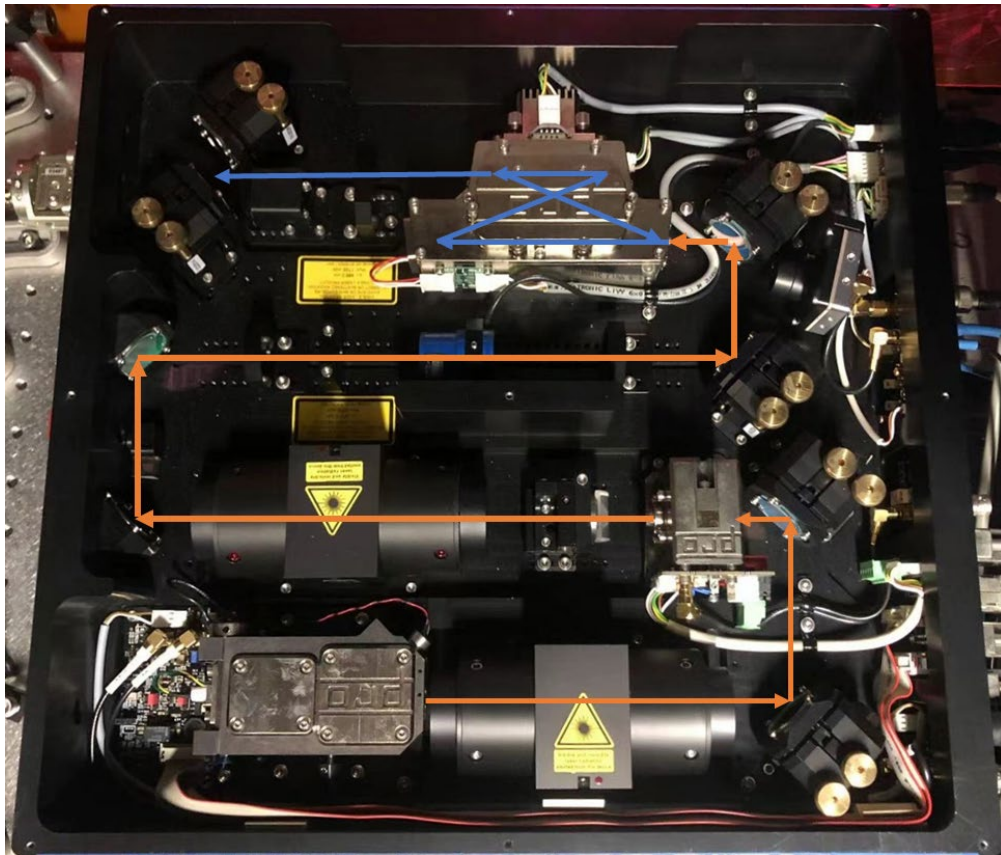
Figure 3.2 Toptica laser internal view

The CW laser source is manufactured by Toptica, Fig 3.2. It comprises a tunable 972 nm extended cavity diode laser (ECDL) amplified by a subsequent tapered amplifier

to 2W. The amplified signal is sent into a second harmonic generation (SHG) ring cavity generating up to 1W of 486 nm laser. All these components are installed on a framework that is hogged out of a single piece of metal to guarantee the ultra-stability of the laser, and the free-running linewidth is < 5 kHz in a 5µs time-delayed correlation.

The SHG cavity resonance is locked to the laser diode's central frequency through fast and slow piezo transducers actuated mirror by Pound-Drever-Hall (PDH) method. An upgrade we have regarding the SHG cavity is that we use an EOM (the blue unit below the Zig-Zag cavity in the picture) to generate the 4MHz modulation required for the PDH technique, instead of directly modulating the current on the 972nm laser, which can induce unnecessary amplitude modulation.

The SHG cavity has a fast frequency response from the stacked piezo structure, in which the fast piezo can respond at up to 13kHz with a 45-degree phase point. Thus the agile frequency tunability of the laser diode can be passed down to the 486nm SHG output.

The major portion of Toptica laser output (580 mW out of 700 mW) is sent through the entrance breadboard optics to the ultrahigh finesse optical interferometer in the spectroscopy chamber. Meanwhile, a sample portion (120 mW out of 700 mW) is sent into an Evanescent single-mode optical fiber going to the ULE cavity, and 93mW can come out from this fiber.

The optics on the entrance breadboard serve two functions: mode-matching to the ultrahigh finesse interferometer with a high power-coupling ratio and generating PDH signals fed back to the Toptica laser for resonance locking. The PDH feedback signals,

both slow and fast, are sent back to tune the Toptica laser frequency. The slow signal drives the tilting angle actuator of the grating in the ECDL oscillator, and the fast signal controls the laser diode current for fast frequency modulation.

By the PDH method, the frequency of the Toptica laser is locked to the sub-kHz vicinity of the interferometer's resonance which can drift with time due to thermal, electrical, or acoustic fluctuation. The laser power can build up to 3-5 kW inside the interferometer and excite 1S triplet-state Ps atoms to 2S states by two-photon excitation. Ps atoms are generated by injecting e^+ atoms into the sample next to the laser beam and then fly across the laser beam at a heavily tilted angle towards the Multiple-Channel Plate (MCP) detector. The laser beam is designed to have a 1mm diameter near the sample for a long interaction time with the particle. A pulsed 734nm laser pulse is simultaneously sent from the top window of the UHV chamber to excite the 2S Ps atoms to Rydberg states. In the 1S-2P experiment, a co-propagating laser pulse containing both 243 nm and 734 nm is used for 1S-2P-Rydberg excitation.

The transmitted optical signal from the interferometer is used to monitor the output power, output mode, and beat with the signal from the reference cavity for instant frequency measurement.

On the reference cavity breadboard, acousto-optic modulators stabilize the frequency of the Toptica laser while compensating the frequency gap between the main interferometer and reference cavity resonances. The fast PDH feedback signal is sent to an AOM for frequency stabilization. At the same time, the slow feedback signal is used to drive a piezo actuator under the front mirror of the main interferometer for cavity

length adjustment and control. Thus we can scan or manipulate the cavity resonance by dialing the RF signal, which drives the AOM acoustic frequency, and the whole system can be automated.

The AOM-stabilized laser is locked to a resonance of the reference cavity, which is made of ultra-low expansion (ULE) glass and set at 58.35ºC, where the thermal expansion coefficient is expected to be zero. The reference cavity transmitting signal is ultrastable with < 25kHz fluctuation. It is an ideal source for frequency comb metrology and the UHV chamber exit signal beating.

3.2   Excitation UHV Chamber

3.2.1   Chamber setup overview
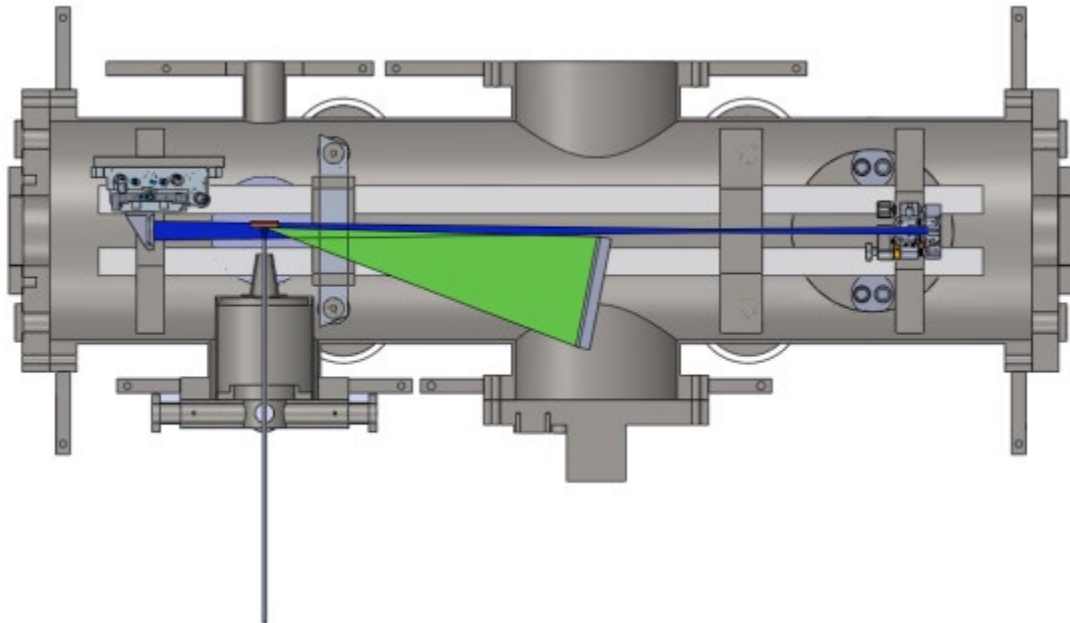
Figure 3.3 Top view of the excitation UHV chamber
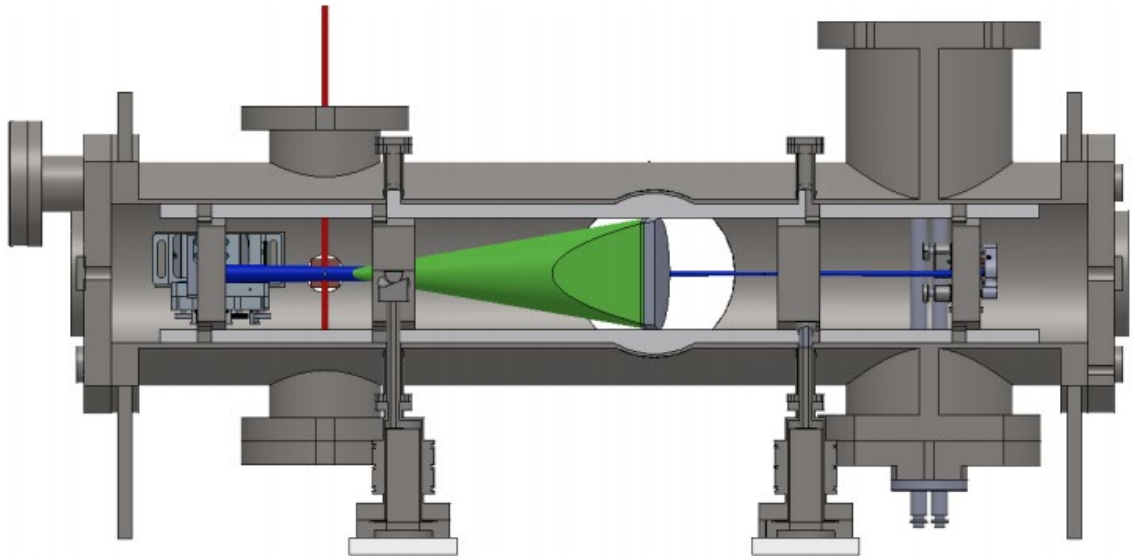
Figure 3.4 Side view of the excitation UHV chamber

A top view of the chamber is shown in Fig. 3.3, and a side view is shown in Fig 3.4. The chamber is 8" in diameter, 1m long, and maintained at 10^{-9} torr vacuum by two 500L/s and one 150L/s ion pump. The positron beam is focused from the Einzel lens to a 0.3 mm region on the angled sample target aiming at the detector. Ps atoms (the green cone) at proper angles will fly across the high-power CW laser (blue beam) built up between the interferometer mirrors at an angle approximately 15° from the laser axis. The angle is chosen such that a Ps atom can spend a long time in the laser beam to reduce the transit time broadening. A 734 nm pulsed laser will be projected from the top window of the chamber, aiming a position after the excitation region along Ps atom trajectories. The timing between the e^+ pulse and the 734 nm laser should be tuned such that the laser pulsed is overlapped with the excited, $n = 2$ Ps atoms. After being excited to 2S states by CW laser and Rydberg states by the 734nm pulsed laser, Ps atoms will reach the MCP plate and be detected.

3.2.2 Optical cavity frame
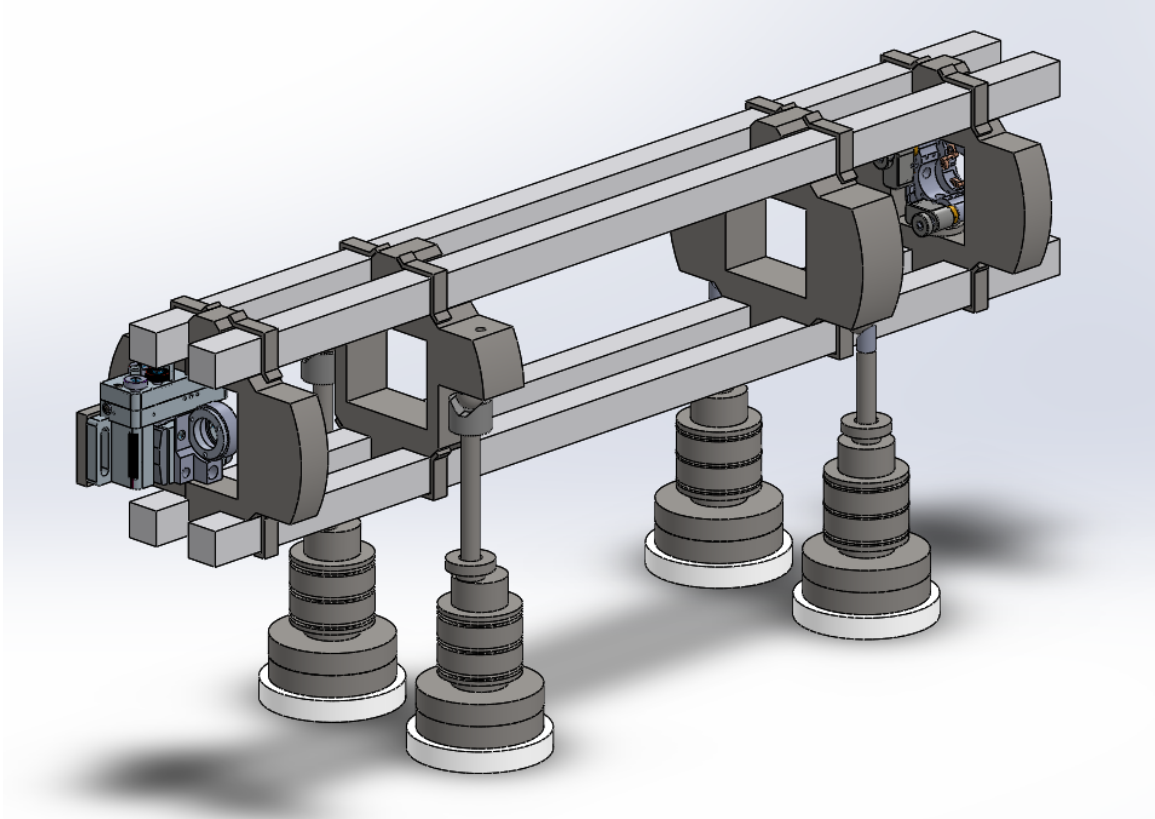
Figure 3.5 Optical cavity frame structure

Fig. 3.5 presents the frame structure where the interferometer mirrors are mounted. It comprises four Zerodur glass rods mounted on four 1" thick stainless steel (SS) plates. A 5-axis picomotor stage (8081-UHV) and a 2-axis (8821-UHV) picomotor mirror mount are fixed onto the SS plates on both ends of the frame, providing flexibility for mirror angle and cavity length coarse adjustment. A fine adjustment of cavity length is provided by the piezo inside the front 20 cm mirror cylinder.

The cavity frame lands through SS balls welded to the 1" plates on a set of kinematic mounts, which allow translational movement and avoid strain on the SS frame

or the glass rods. The mounts consist of two V-shape grooves and two slanted surfaces facing each other, forming the third groove, fixed on top of four posts. The pedestal flanges of the four posts are secured directed onto the optical table surfaces, while their connections to the chamber wall are by welded bellows. The connection between the posts' pedestal flange and the table surface is through 0.6" thick Peek pads to guarantee mechanical strength and thermal insulation between the cavity and the table surface. The Peek pads also protect the table surface from overheating locally when baking the chamber. Thus the acoustic noise on the chamber wall is attenuated from coupling to the table surface and consequently the optical cavity.

To reduce static charge accumulation, silver paint is applied to the Zerodur glass rods to ground them through the SS plates.

3.2.3 Optical cavity mirrors

We designed a cavity with a large diameter beam ($\omega = 0.942$ mm) at the region where Ps is excited to reduce transit-time broadening. A 1" diameter $R = 50$ cm and a 0.5" diameter $R = 20$ cm concave mirror facing each other at a distance close to but less than 70 cm are used to form the interferometer. The closer this distance is to 70cm, the larger the beam expands, but the more sensitive the cavity is to any vibration. A trade-off has to be made between a large beam size, which reduces transit time broadening and benefits thermal performances, and the robustness of the cavity, which determines the frequency stability. With a proper setup of the UHV mirror mount and the 5-axis stage, the cavity length is adjustable between 69.20 cm and 69.50 cm.

The cavity length can be measured to the second digit after the decimal by measuring the divergence of the cavity output beam. A recent measurement indicates that the current cavity length is 69.26cm.

Due to the extreme sensitivity to noise and the thermal effect induced by the high build-up power, the mirror mounts are designed with precaution. The front and rear mirror mount designs are demonstrated below.
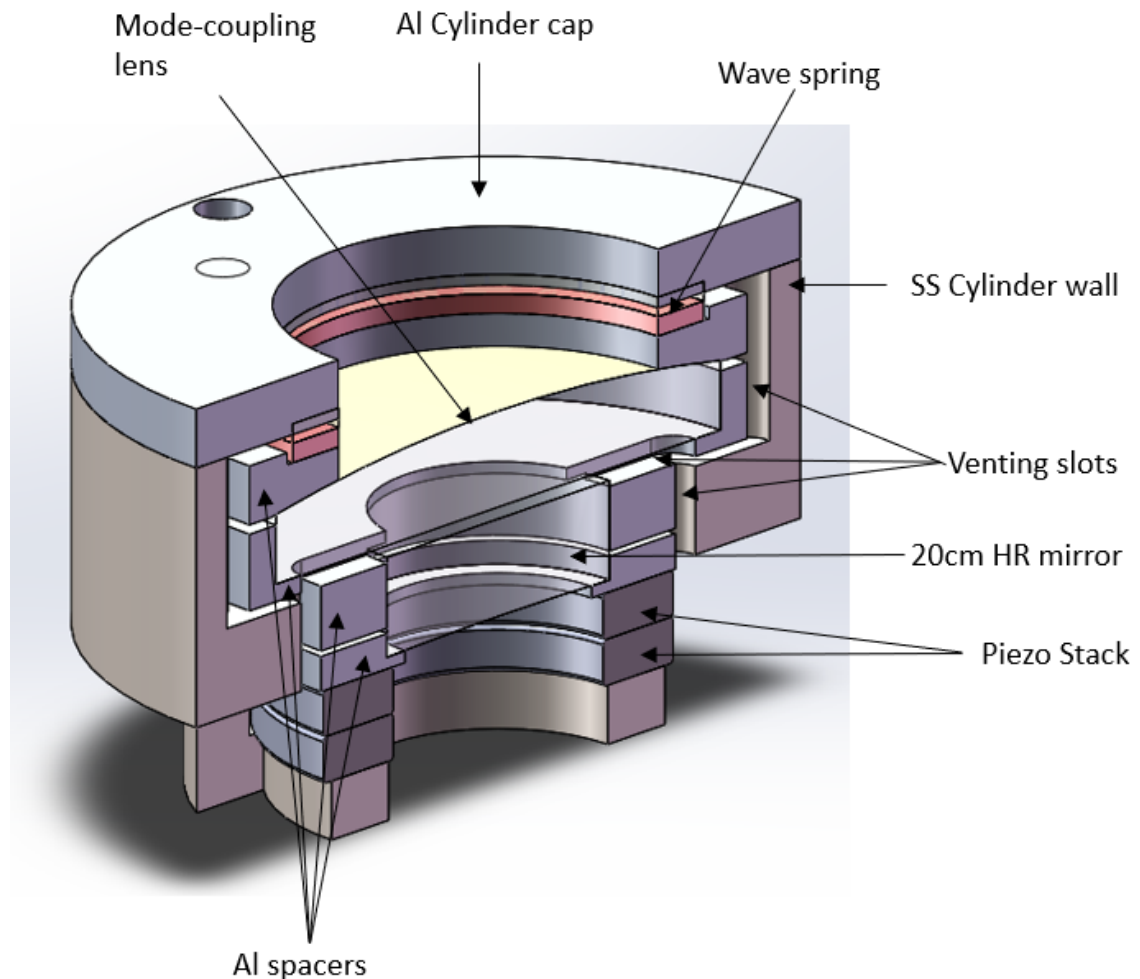
Figure 3.6 d=0.5" R=20 cm front mirror cylinder

Fig. 3.6 is a cross-section view of the front mirror cylinder. The materials must be selected carefully to avoid cold welding in a UHV environment, as sliding movement is required by cavity length fine adjustment, and venting slots have to penetrate through the whole structure to prevent possible degassing after installation.

A mode-coupling lens is stacked in front of the mirror to generate the highly convergent beam required by the cavity. Two ring-shaped piezos are stacked under the HR surface of the 20 cm mirror, and the whole internal set is pushed against the piezo stack by a wave spring backed by the cylinder cap. When a voltage is applied to the piezo stage, the mirror can move along the cylinder's axis, resulting in a fine length adjustment of the optical cavity. The piezo's voltage is a combination of the PDH feedback signal, a ramping voltage, or a DC voltage from a SRS SIM928 floating battery.
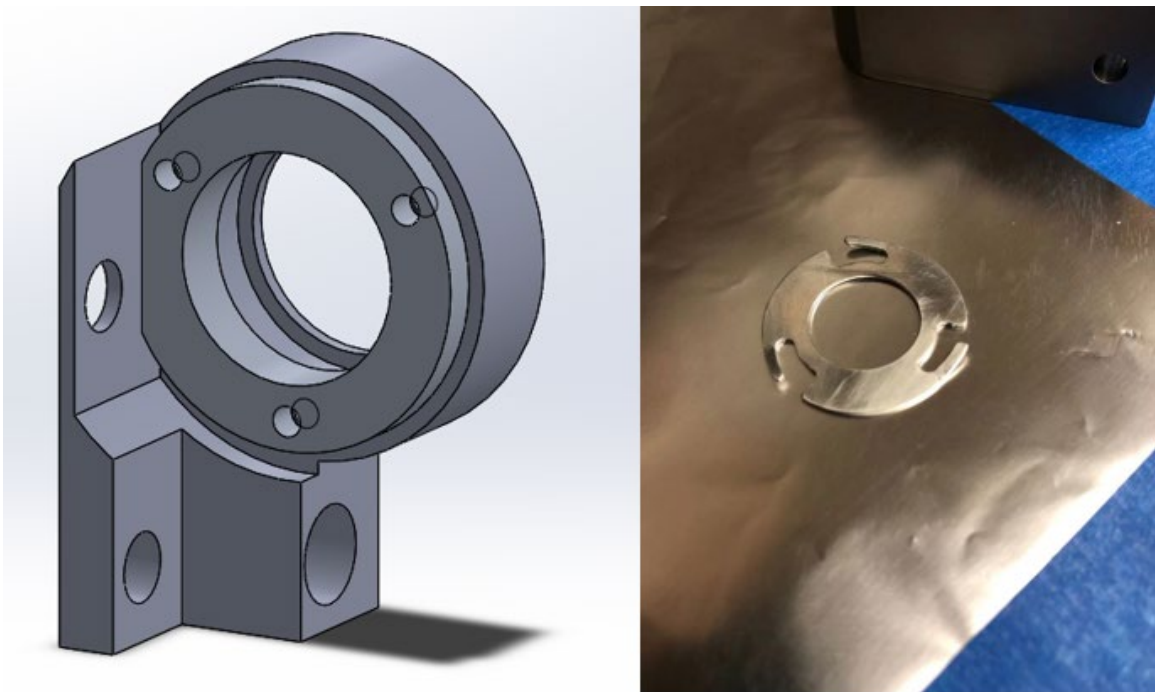
Figure 3.7 d=1" R=50cm rear mirror cylinder

Fig. 3.7 left shows the rear mirror mount for the 1" R=50cm concave mirror. Compared with the d = 0.5" counterpart, the 1" optic has less rigidity. The mirror could be easily distorted by excessive or unevenly distributed mechanical force. Possible sources of this force are tightly squeezed wave spring, rough surface on the supporting rim, or lack of room for thermal expansion, especially under thermal effect induced by the high-intensity Gaussian beam. The mirror distortion is manifested by the deterioration and fluctuation of the cavity output mode shape and power. Fig. 3.8 shows two cases of corrupted cavity modes. They look like multiple TEM_{nm} modes overlapped, where n and m could be as high as 30. Due to the competition of different TEM modes embedded, the output power could experience an intensity drops up to 30% and power fluctuations up to 15%
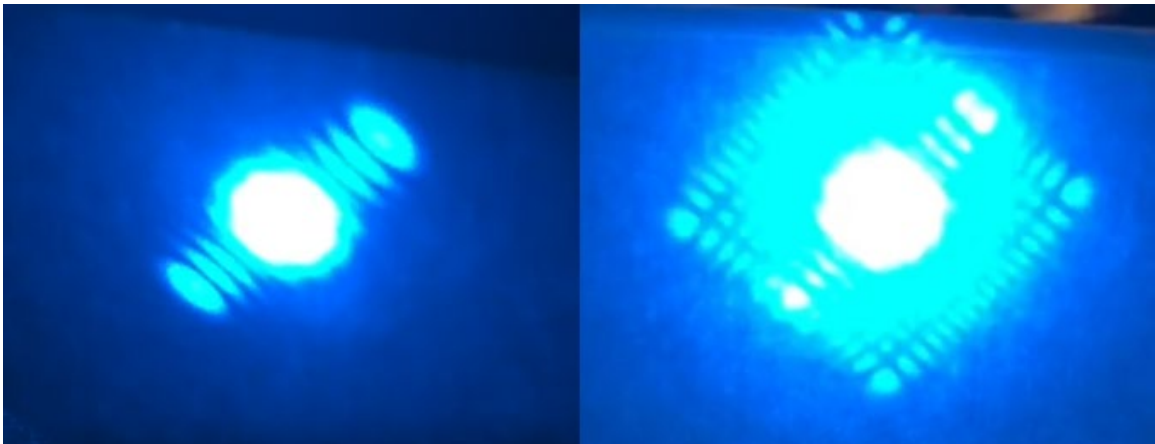
Figure 3.8 Deteriorated cavity mode due to mirror distortion.

Fig. 3.7 right shows a tension relief spring that can help fix this issue. The spring is a 0.7 mm thick aluminum plate with three thin flipped-up arms providing only several

grams of force to the inner edge of the optic. Moreover, the mirror mount has to be pocketed at a larger diameter to allow thermal expansion movement of the mirror.

3.2.4 Cavity finesse and circulating power

An ultrahigh finesse cavity can benefit Ps 1S-2S excitation on two aspects. First, a higher finesse means a sharper linewidth which reduces the errorbar in frequency measurement. Second, it also means a higher build-up power for a higher excitation rate. The finesse of a Fabry-Perot interferometer is defined to be the ratio between the free spectral range (FSR) and the FWHM of each resonance peak. The FSR is defined by $2L/C$, where L is the cavity length and C is the speed of light. Thus for a cavity of a certain length, high cavity finesse means sharp resonance peak width and less uncertainty.

The finesse of a cavity is correlated to the reflectivity of the mirrors by equation 3.1, where the denominator is the total power loss of the two mirrors. T_i represents transmission loss, L_i represents all other losses, including scattering and absorption, and the subscripts indicate the mirror they represent.

$$\mathcal{F} = \frac{2\pi}{T_1 + T_2 + L_1 + L_2}$$

Equation 3.1

The total loss of the mirrors also determines the ring-down time of the optical power stored in the cavity when the input is suddenly cut off by equation 3.2, where L is the cavity length and C is the speed of light.

33

$$\tau = \frac{2L}{C(T_1 + T_2 + L_1 + L_2)}$$

Equation 3.2

Combining Equation 3.1 and 3.2, we can calculate the finesse of a cavity by the ring-down time with equation 3.3.

$$\mathcal{F} = \frac{\pi C \tau}{L}$$

Equation 3.3

The Advanced Thin Films mirrors we use in our interferometer have an RMS roughness < 1 Å, and the specified transmission loss is <30ppm (finesse>100,000) for each mirror. However, the scattering and absorption loss can increase with time due to carbon compounds depositing on the reflective surface of the mirror. The mirror reflectivity can be restored by leaking ten torrs of oxygen into the chamber and turning on a pair of UV lamps inside the chamber for 15 min. The carbon compound can be cracked, oxidized, and subsequently sucked out of the chamber by a turbopump. Seven repeated O_2 and UV treatment processes can increase the ring-down time from 24µs to 44µs, with the total loss exponentially decayed and stabilized to 108 ppm, indicating a cavity finesse of 5.9×10^4. If we assume $T_1 = T_2 = 30$ppm as specified by the vendor and $L_1 = L_2$, then the scattering and absorption loss averaged on each mirror is 24ppm. However, in the actual case, this assumption may not hold as the condition for each mirror may be different. Providing our cavity is 0.6926m long, the FSR is then ~216 MHz, and the FWHM of its resonance is approximately 3.7 kHz. With PDH locking

technique, the laser frequency can be locked to the center 5% of a resonance peak of the interferometer. In our case, the uncertainty from locking is less than 200Hz

High finesse is also critical for the generation of high circulating power. We use two-photon excitation to eliminate the first-order Doppler shift effect. However, two-photon excitation has a much smaller cross-section than single-photon transition, and the transition rate scales with I^2 where I is the field intensity.
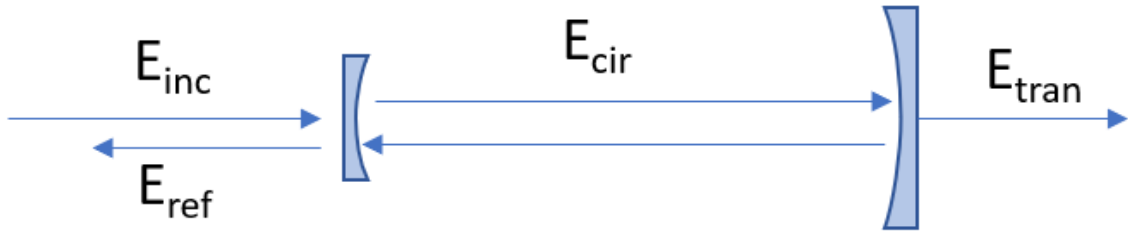
Figure 3.9 Field of a Fabry-Perot interferometer

$$E_{cir} = \frac{t_1}{1 - r_1 r_2} E_{inc}$$

Equation 3.4

When the incident beam is on resonance, the circulating power of a Fabry-Perot cavity can be calculated by equation 3.4, where t_i and r_i are the transmission and reflection coefficients for the electric field. Their squared values, $t_i^2 = T_i$ and $r_i^2 = R_i$, are the power coefficient, and the conservation of energy requires $T_i + R_i + L_i = 1$. Based on the transmission loss and reflectivity we measured above, we could achieve up to 5 kW circulating power inside the cavity with 500 mW incident power if perfect mode-matching could be achieved. However, in an actual case, the estimated (with the assumption that $t_1 = t_2$, $r_1 = r_2$) best power coupling efficiency we acquired is 89%. And

the long-term high circulating power will result in a thermal deformation of the mirror surface. Although the beam profile can be maintained Gaussian if the deformation is symmetric, the mode coupling efficiency may drop.

3.2.5   Entrance breadboard
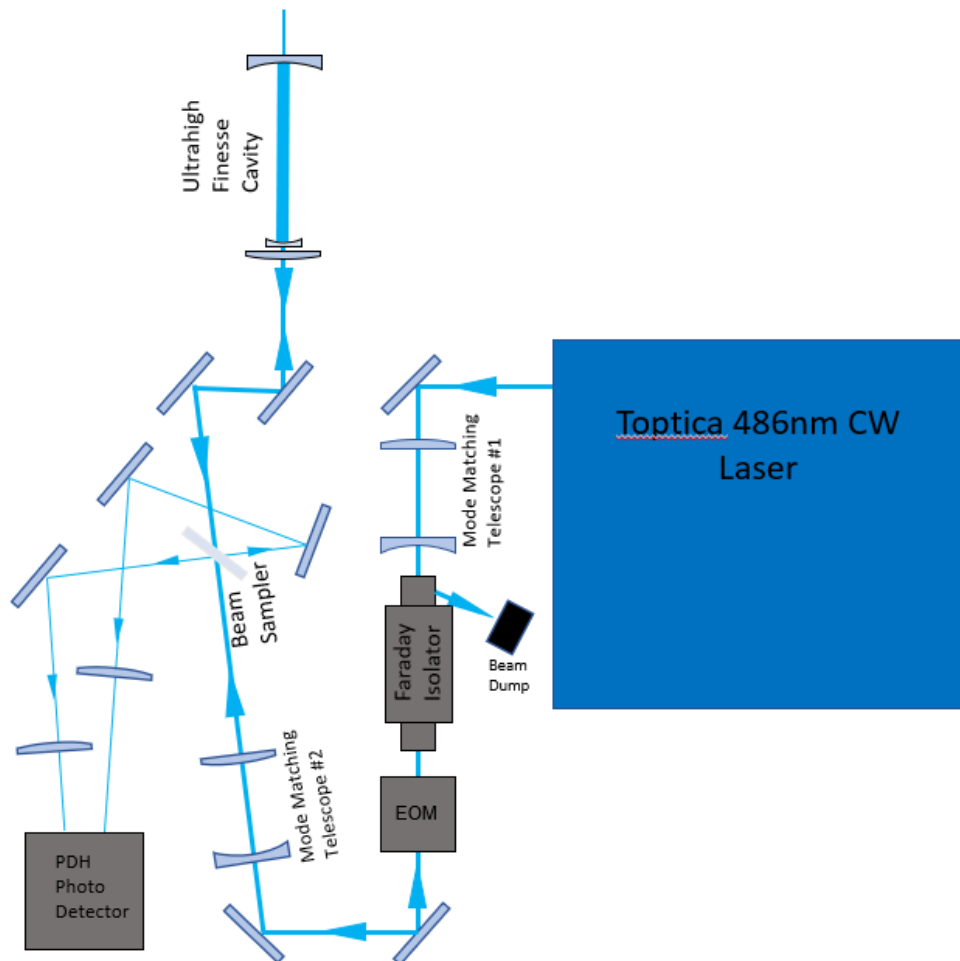
Figure 3.10 Schematic of the entrance breadboard

The entrance breadboard serves two functions: PDH locking [81] and mode-matching. Its design is shown in Fig. 3.10.

The electro-optic modulator can generate a 50 MHz phase modulation on the incident beam, which is equivalent to adding two sidebands ±50 MHz away from the central frequency. The modulated beam is sent to the interferometer. Sample beams from the incident and reflected beams are deflected and sent into two distinct channels of the Thorlabs PDB450A-AC photodetectors. A positive lens is inserted in each sample beam path at one focal length away from the input aperture, adding robustness against fluctuation due to acoustic or thermal drift. The error signal generated by PDB450A-AC is multiplied by the 50 MHz modulation function in a Topitca PDD110 mixer and filtered by a FALC110 to generate a feedback signal to the Toptica laser.

The optical beam directly out of the Toptica laser is collimated with a 700 μm waist size, but the interferometer required input is a highly convergent beam of a different size. Except for the mode coupling lens in the 20cm mirror cylinder, two telescopes are also set on the entrance breadboard to provide two degrees of freedom to adjust the input beam convergence and beam size. The coupling efficiency could be estimated through equation 3.5, assuming $T_1 = T_2$ and $l_1 = l_2$ [82]. To tell the difference between T_1 and T_2 or $l_1 = l_2$, it is also necessary to characterize the optical cavity with the laser beam incident reversely into it.

$$\frac{P_{tran}}{\epsilon P_{inc}} = 4 T_1 T_2 \left(\frac{\mathcal{F}}{2\pi}\right)^2 = T^2 \left(\frac{\mathcal{F}}{\pi}\right)^2$$

$$\frac{P_{ref} - (1 - \epsilon) P_{inc}}{\epsilon P_{inc}} = (l_1 + l_2 + T_1 - T_2) \left(\frac{\mathcal{F}}{2\pi}\right)^2 = l^2 \left(\frac{\mathcal{F}}{\pi}\right)^2$$

Equation 3.5

It is worth noting that due to thermal expansion induced by the high circulating power, when the laser is locked to the cavity, the required mode would drift and reach an equilibrium after approximately 30 min. The design of the telescopes has to take thermal effects into consideration. An optimized mode-coupling setup for the initial pre-heating condition will lose its mode-matching efficiency significantly after the thermal effect. Nevertheless, a mode-coupling design optimized for the post-equilibrium state may not initially couple in enough power to allow the cavity to reach the thermal equilibrium point for which it is designed. A trade-off is made, and a estimated maximum 89% mode coupling efficiency can be achieved after the thermal equilibration.

3.2.6 Exit breadboard
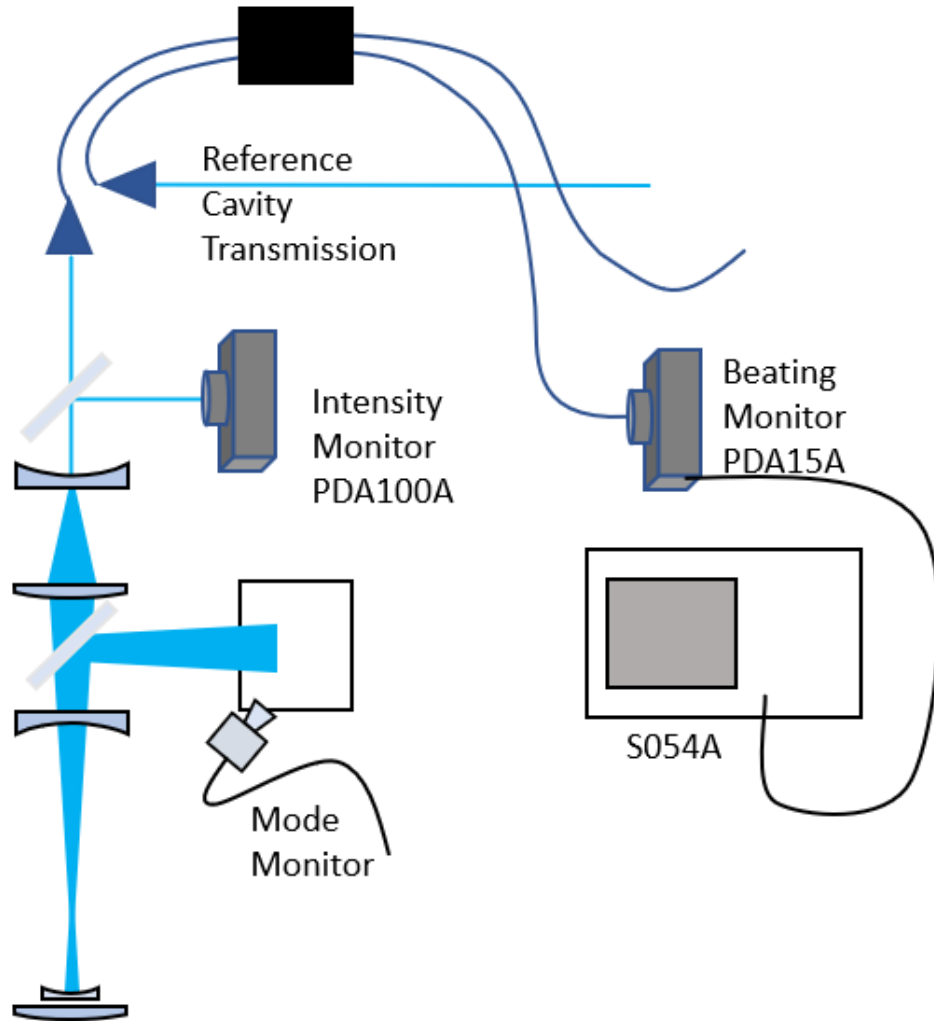
Figure 3.11 Schematic of exit board of UHV chamber

The schematic of the exit board is demonstrated in Fig. 3.11. The cavity output is

a highly divergent beam with a large beam width. A sample of this beam is projected

onto a white screen, and the image is recorded by a camera to monitor the mode quality.

The rest of the beam is shrunk down and collimated by a telescope. Part of this beam is

sent into a PDA100A to monitor the output intensity of the interferometer, and the other

portion is sent into an Evanescent fiber coupler to beat with the frequency-shifted and

frequency-stabilized signal from the reference cavity transmission. The beating signal is

detected by a PDA15A photodiode with a 350MHz bandwidth and recorded by a

Keysight S054A oscilloscope with a sample rate of up to 20 GSample/s.
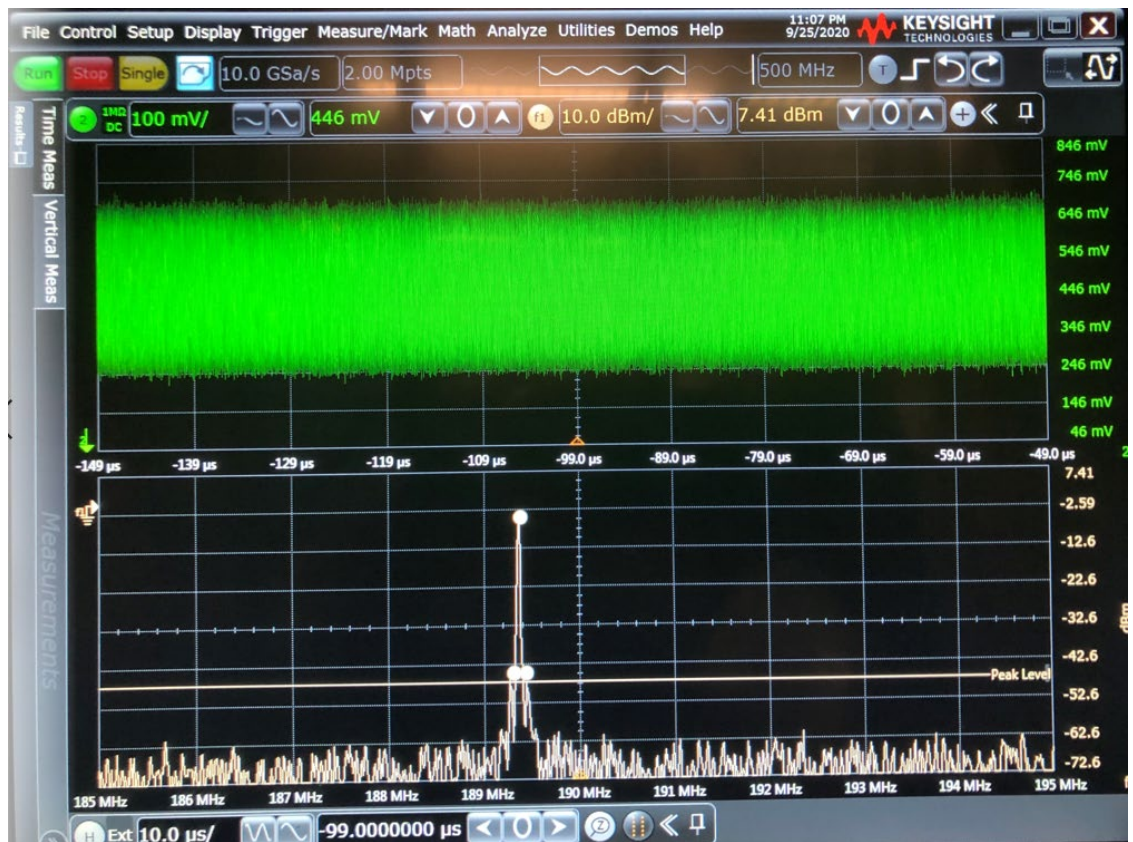
Figure 3.12 Beating signal between UHV cavity output and reference cavity

A 100 μs window before and after the Ps excitation event will be recorded to

analyze the instant frequency of the laser. A sample window is shown in Fig. 3.12. The

top half window shows the beating signal with a peak-to-valley size of 450 mV, while the

peak value is at 700 mV. The bottom half window shows an FFT of the beating signal

with a central peak at 189.3 MHz. This frequency is determined by the AOMs on the

reference cavity breadboard and can be adjusted or scanned automatically by computer programs. The AOM frequency modulation will be discussed in detail in section 3.4.

3.3   Noise Insulation

As calculated in section 3.2.4, the ultrahigh finesse cavity has a resonance of only 3.7kHz wide. However, the noises the cavity picks up from the environment can generate a much larger resonance jitter. For the 486 nm and 0.7 m long interferometer, a 243nm half-wavelength drift is correlated to a 216 MHz FSR, and a 3.7 kHz frequency drift can be caused by only a 4pm cavity length change. The resonance jitter from ambient noise pick-up is much larger than the 3.7 kHz FWHM. Several noise-insulation techniques are adopted to suppress the jitter.

There are three main sources of noise: thermal, electrical, and acoustic. An enclosure, with metal frames and walls for electrical insulation and foam mounted on the walls for thermal and acoustic insulation, was built around the optical table. The thermal drift is suppressed by controlling the environment temperature of the enclosure with a ThermoTEC 161B air conditioner and RTD sensors, and the temperature is stabilized to $72.0 \pm 0.1°F$ by a PID control system. However, with laser power circulating, both interferometers can experience thermal drift once the laser is locked. As we only care about the instant frequencies within the 100μs window around Ps excitation event, which are recorded with optical beating or Frequency comb counter respectively, these drifts do not significantly affect the uncertainty.

Electrical noises come from the ground loops, which are at 60 Hz and its harmonics, and electromagnetic waves picked up by coax cables. The ground loop noises

are avoided by designating a common ground for all electrical devices and eliminating redundant electrical contact by applying insulation layers between chassis. Floating battery power supplies are also adopted to drive critical sensing devices like the PDB450A-AC photodetectors or piezo stack. Tripple-layer coax cables are used for better EM wave shielding, and 15dB BNC attenuators inserted between coax endings and device inputs further suppress the pick-up signal on the cable, while useful signals are not affected by tuning up the gain. Some solenoids of the Ps beamline are turned on only before firing positrons to avoid heat accumulation. The large derivative of this magnetic field will excite an EM wave detected by all electrical sensing devices. To avoid interference with the experiment, magnets are ramped up more than 10ms before the Ps pulse.

Compared with the two sources above, acoustic noise has the most significant impact on the resonance jitter. We took several approaches to suppress acoustic interruptions. Floating legs of the optical table and isolating tires under the UHV chamber frame reduce the noise coupled to the cavity[22]. We used an accelerometer to analyze the spectrum of the mechanical vibrations coupled onto the optical table surface, and the vibration amplitude detected on the vibration chamber is approximately 1 nm. Meanwhile, the vibration on the optical cavity indicated by the frequency jitter is less than 0.5 Å

Other than the legs and tires, we installed an insulation cover above the entrance breadboard, the frame of which is fixed on the enclosure framework and has no contact with the table surface. Four-inch thick wedged acoustic foam is also attached to all

surfaces of the enclosure and the insulation cover boards, as shown in Fig. 3.13. The air conditioner fans are customized for a quieter and more gentle airflow, as in Fig. 3.14.

Three peaks show up around 180 Hz, 600 Hz, and 980 Hz, respectively, on the spectrum of the feedback signal to AOM, and no peak shows up above 1000Hz. The entrance board cover and enclosure wall can each reduce about 10dB noise showing on the feedback signal spectrum. A spectrum is shown in Fig. 3.15.

Figure 3.13 Acoustic insulation structure.

Figure 3.14 Ultra quiet fans for air conditioner.

Figure 3.15 Double locking and feedback signal frequency spectrum

3.4 Reference Cavity Breadboard

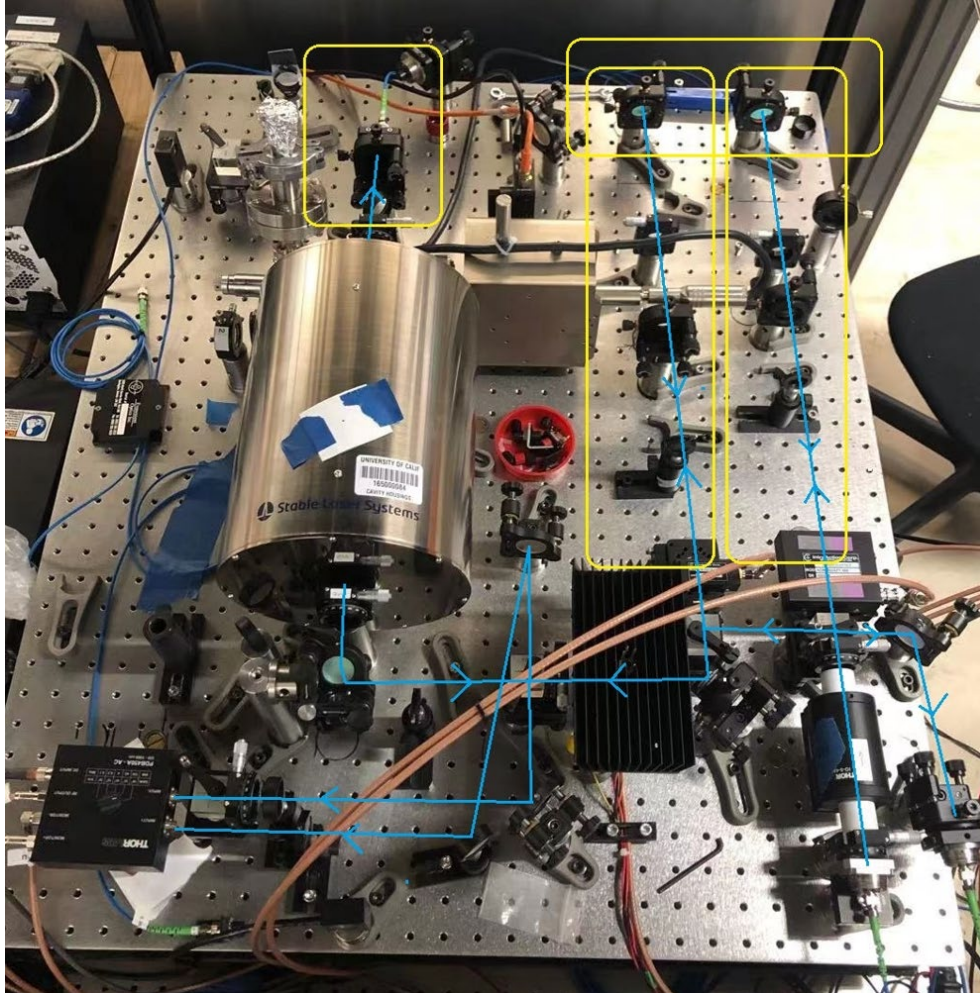Figure 3.16 Reference cavity breadboard layout

Despite all the noise suppression efforts, a resonance jitter with an amplitude of 60kHz (0.68Å in cavity length) is still observed on the main interferometer. To perform precise frequency measurement for Ps excitation, we set up a frequency stabilizing system by acousto-optic modulators and lock the stabilized laser beam to an ultra-stable reference cavity.

The layout of this breadboard is shown in Fig. 3.16. Blue lines in the figure demonstrate the beam path of the 486nm laser. Approximately 120mW of the Toptica laser is sent to the reference breadboard through an Evanescent single-mode fiber, and 95mW comes out. A Faraday isolator is set immediately out of the fiber output coupler to avoid potential back reflection from the following beam path. The beam is then Bragg scattered by an 80 MHz AOM. The first order is selected out by an aperture, transmits through a lens set one focal length away from the deflection point, then reflected by a mirror at the Gaussian waist. A lambda/4 wave plate is set before the mirror to rotate the polarization by 90 degrees after a double pass, and a beam splitting cube is used to reflect the backward beam into the following path. Then the retroreflected beam is Bragg scattered again by the AOM and sent into the second AOM branch. A similar procedure occurs in the second 200MHz AOM, and the double passed beam will be sent through PDH optics, then to the reference cavity. The fast PDH feedback signal drives the 200 MHz AOM to lock the laser to reference cavity resonance, and the slow feedback drives the UHV cavity piezo so that the cavity length can be scanned by detuning the AOM frequency. The 80 MHz AOM is set at a constant value to compensate for the residual difference between the UHV and the reference cavity.

We use the first-order Bragg deflected beam, which is shifted by the same frequency as the acoustic wave propagating in the crystal, as the power efficiency of the first order is much larger than other orders. For optimized power efficiency, the deflection angle of the first-order beam of an AOM output depends on the designated

acoustic frequency by equation 3.6, where λ is the optical wavelength, d is the acoustic

wavelength, and θ is the angle between the optical beam and acoustic wave plane.

$$\lambda = 2d\ sin(\theta)$$

Equation 3.6

For our application, we need a fast modulation and a long-range scan of the AOM

frequency, and we choose the 200 MHz AOM because the first order efficiency can be

well maintained within a long tuning range (-10 MHz ~ +35 MHz, single-pass).

Under fast modulation, the deflection angle of the first order beam also oscillates

rapidly. To maintain the alignment, we use a cat's eye system formed by a lens and a

mirror [83], which is circled by yellow squares in Fig. 3.16. Ideally, the deflection point

is regarded as fixed under different modulation frequencies and is set on the focal point

of the positive lens. Thus the lens output beam maintains parallel to the optical axis.

When this output is normally reflected by the mirror, it propagates back along the same

path, and after a second first-order AOM shift, the deflection angle will be compensated

back to zero.

This ideal cat's eye model works well when alignment requirement is not critical.

However, in our application, we need to align the beam to a reference cavity.

Misalignment will sensitively result in a change in mode coupling efficiency, leading to

an intensity modulation of the reference cavity output beam and consequently frequency

modulation, which will deteriorate the stability of the reference signal. So besides laying

the frequency modulating AOM branch closer to the cavity to reduce the misalignment

magnified by beam path length, we conducted further studies on the AOM performance

and the design of the cat's eye system, and the angle fluctuation is reduced to < 5 micro radians within the 45 MHz single-pass or 90MHz double-pass frequency scan.
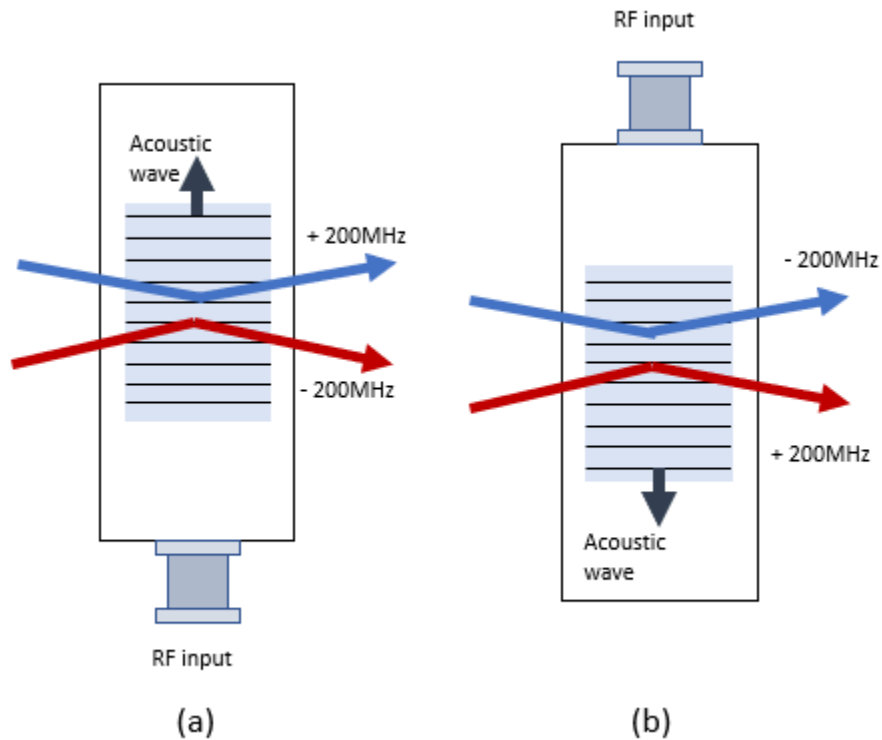
Figure 3.17 Laser beam deflection of an AOM

Fixing the AOM acoustic frequency, the power in the first-order deflection can be optimized in two directions depending on the angle between the laser beam and AOM, as shown in Figure 3.17 (a). Blue and red arrows represent two options of deflection direction between a laser beam and the AOM, and the correlated frequency shift is labeled. However, if an experiment requires a long-range frequency scan, only one option is applicable, depending on the model of the AOM. Since the angle between the laser beam and AOM is usually optimized for the first order power of a specific frequency, when the frequency is detuned, efficiency drops will occur, and one of the deflection

directions will experience an efficiency drop more severe than the other. For example, with the blue arrow setup, the 200MHz IntraAction AOM used in our experiment maintains the first order power within 5% within the 45MHz frequency scan, while with the red arrow setup, the first order power drops to 60% of the optimized value with only a 5MHz detuning. If a flip of the frequency shift direction is intended, the AOM must be flipped by about 180 degrees while conserving the deflection direction, as shown in Fig. 3.17 (b).

Besides efficiency drop, an "aberration" effect of the Bragg scattering also needs to be noticed. The cat's eye model described above assumes a fixed deflection point under frequency detuning. For precise alignment maintenance, this approximation does not hold anymore. A careful examination of the AOM deflection angle demonstrates that the deflection point shifts along the beam axis when the AOM frequency is detuned from the optimized value.

Fig. 3.18 shows this transition of the 80 MHz AOM. The green line overlapping the X-axis represents the deflected beam path when the AOM alignment is optimized at 80 MHz, and the blue and the yellow line represents the beam path when AOM is detuned to 84MHz and 76MHz, respectively. The deflection point transition of ~4cm was observed.

49
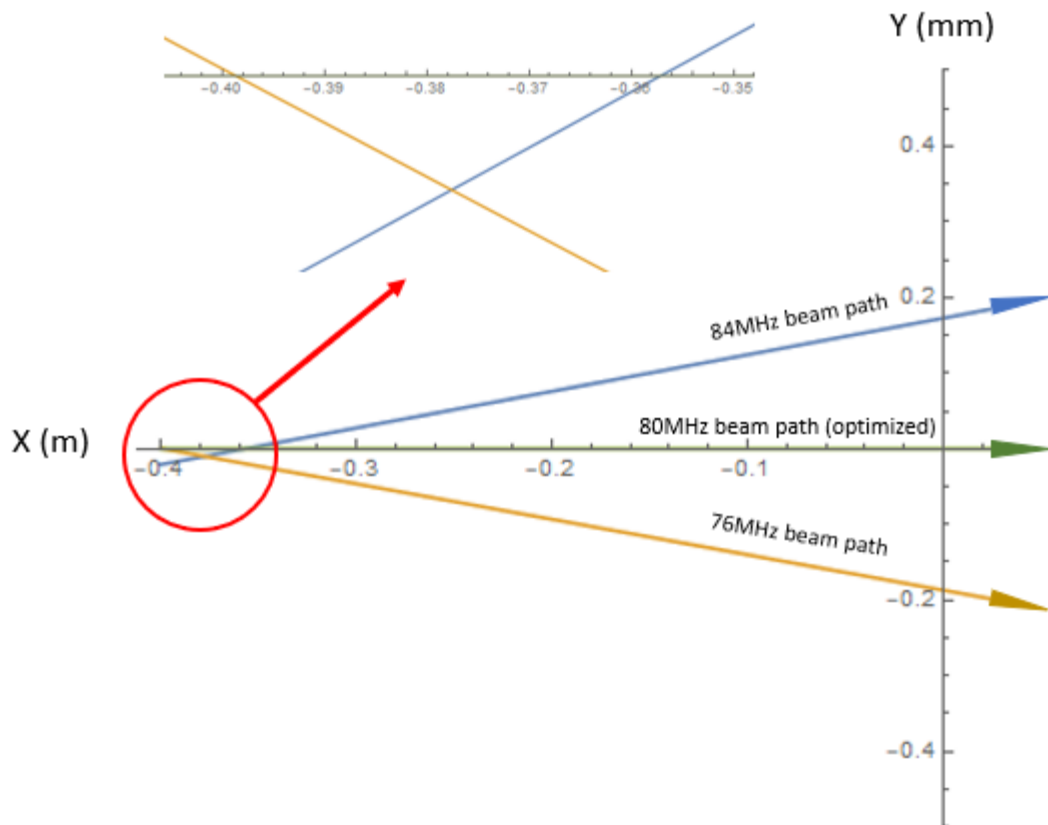
Figure 3.18 Deflection point transition along the beam axis.

A common solution is to use a lens with a long focal length. However, this method only reduces the error proportional to the reciprocal of the focal length. Due to the apparatus setup and the lens availability on the market, the power of this method is limited, especially for precision alignment requirements. Here we present two approaches to reduce the uncertainty in the alignment further.

First, AOM with a larger frequency usually possesses a smaller deflection point transition for the same frequency detuning value. For a specific modulation value, two AOMs shifting to opposite directions could be used, and the large frequency modulator could be used for scanning. For example, to shift the beam by 240 MHz, we use 200MHz

and 80MHz double-passed AOMs instead of a single 120 MHz AOM and take advantage of the long scanning range of the 200MHz AOM.

Second, the deflection point transition geometry is similar to the spherical aberration of a plano-convex lens. The aberration effect close to the edge of such a lens could generate a parallel-to-axis beam. The lens curvature must be carefully selected, and the angle between the lens axis and AOM first-order beam must be set precisely.

The lens also re-defines the Gaussian beam profile. To guarantee that the retro-reflected beam from the mirror goes through the same optical process, the cat's eye mirror needs to be set on the waist of the lens output beam. Gaussian optics require another waist to appear at the front focal point of the cat's eye lens, which also improves the AOM Bragg scattering efficiency. Nevertheless, the waist size must be carefully adjusted for AOM efficiency, mode quality, and a beam profile that benefits the following path. After hard efforts, our AOM branches can harvest 16 mW out of 80 mW input power and maintain alignment within five micro radians for a 90 MHz frequency scan, paving the way for the reference cavity locking.

With the alignment maintaining frequency modulation and scan system, we significantly improved the locking quality to the reference quality. The drop-out percentage decreased from 20% [22] to 4%, reducing the uncertainty of the reference frequency to less than 1 kHz. Fig 3.19 shows a ULE locking line within a 200μs window, and the min/max = 96.9%. In the middle of the oscilloscope window is a dip which shows the exponential decaying and the recovery of the cavity transmission intensity due to the temporal off-resonance of the incident beam, which we call a drop-out. The drop-

outs are caused by a too fast dF/dt that the AOM compensation can not trace. Note that the drop-out noise strongly depends on the UHV cavity resonance stability, and the > 96% double-locking (UHV and reference cavity) could only be achieved from a combined contribution from noise insulation and frequency stabilizing systems. Fig 3.20 shows the spectrum of noise on the transmission signal. In contrast to the 48dB noise on the feedback channel shown in Fig. 3.15, the noise on the transmission signal is suppressed to <5dB above the background noise with only a 5dB peak at 180Hz and a 10dB peak at 530Hz, where the ground loop noise and strongest acoustic noise are located.

The 16 mW input to the reference cavity generates a 2mW transmission power and guarantees the need for intensity monitoring, frequency comb, and UHV exit board beating. The drop-outs can cause an amplitude modulation on the ULE transmission signal. However, as the acoustic noise is practically zero above 1000Hz, the uncertainty induced by the amplitude modulation is no more than 1Hz.
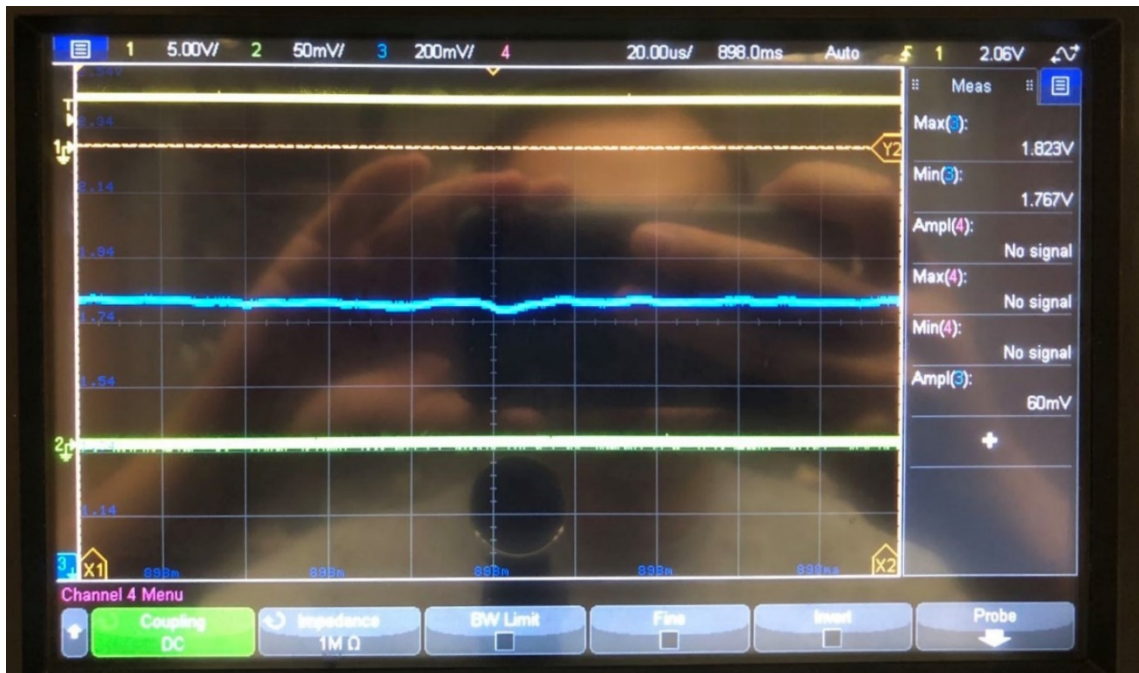
Figure 3.19 ULE transmission signal within a 200μs window
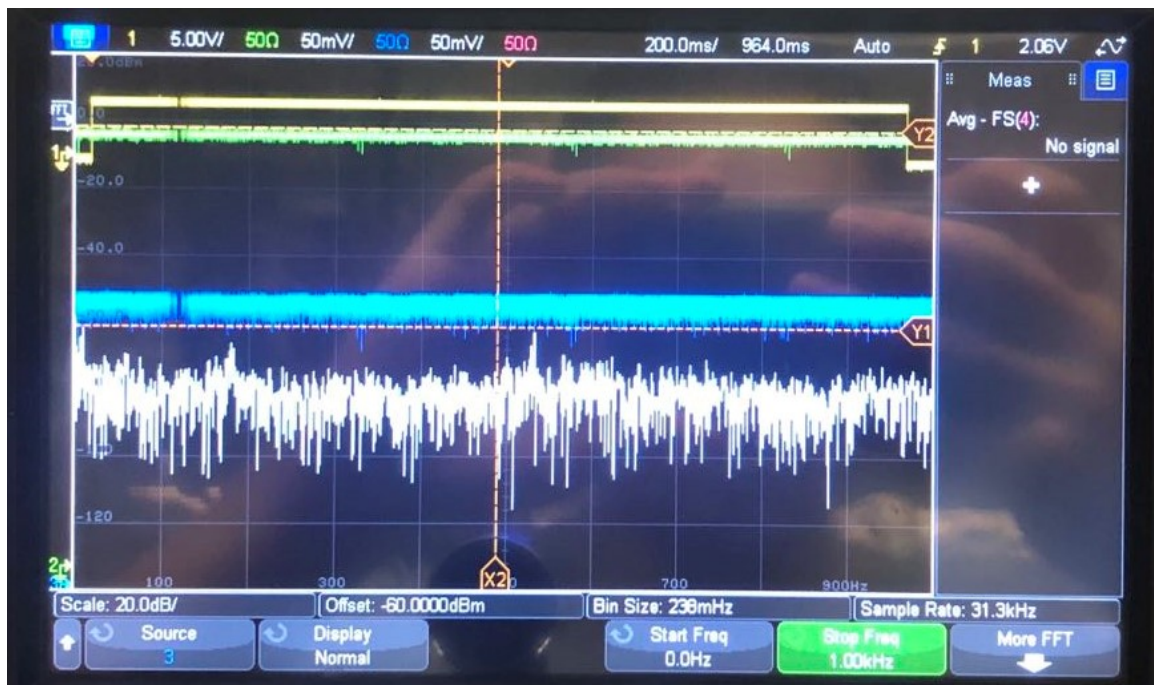
Figure 3.20 ULE transmission noise spectrum

3.5   Frequency Comb

The frequency stabilized optical signal is sent to a frequency comb, a laser-based metrology device whose spectrum comprises equally spaced, discrete frequency peaks, as shown in Fig. 3.21. The frequency peaks are separated by a value called repetition frequency f_{rep}, and the zero offset is carrier envelop offset f_{ceo}. In a frequency measurement, one comb tooth is selected to beat with the optical signal, and the beating frequency f_{beat} is recorded. The frequency is given by equation 3.7, where N is an integer that needs to be decided.

$$f_{cw} = N f_{rep} + f_{ceo} + f_{beat}$$

Equation 3.7
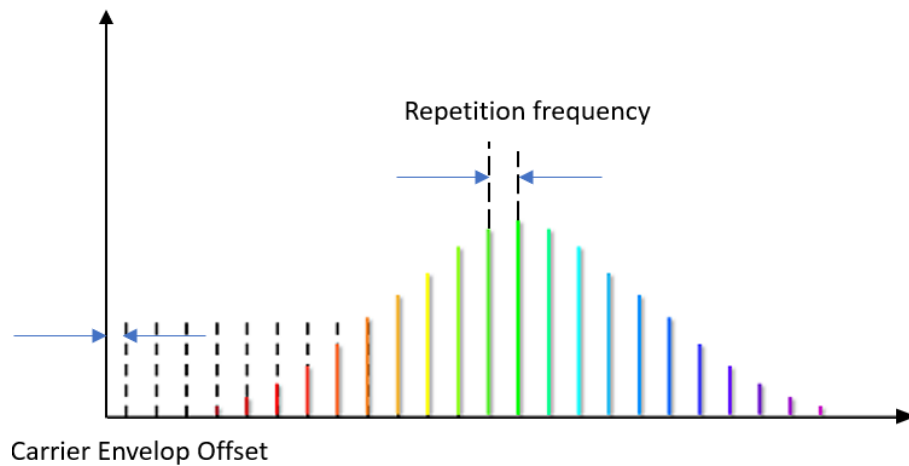
Figure 3.21 Frequency spectrum of a frequency comb.

The frequency comb we use is the FC1500-250-ULN model manufactured by Menlo Systems. The laser source is a mode-locked, femtosecond erbium-doped fiber laser (EDFL) whose peaks center at 1560nm and span by approximately 25 nm. The

repetition rate is finely controlled and tunable at around 250 MHz. The laser source is

sent into a nonlinear fiber which octave spans the spectrum to a range that covers 1 μm ~

2μm. In the spanned spectrum, one peak on the red side is frequency-doubled and beat

with another peak on the spectrum with twice as much frequency, and the beating

frequency reflects the frequency of the CEO. This procedure is shown in equation 3.8.

$$f_{red} = Nf_{rep} + f_{ceo}$$

$$f_{blue} = 2Nf_{rep} + f_{ceo}$$

$$2f_{red} - f_{blue} = 2Nf_{rep} + 2f_{ceo} - 2Nf_{rep} - f_{ceo} = f_{ceo}$$

Equation 3.8

The broadband, frequency-doubled beam is output from the laser box into free

space. However, its frequency span does not cover the 486nm wavelength we need for

the CW laser. So this beam is sent into a Photonic Crystal Fiber (PCF), which has a high

nonlinear effect and expands the frequency span to the wanted range, and a blue filter is

used to pick out the desired wavelength signal and send it into a fiber coupler to beat with

the reference cavity output signal. The mixed beating signal is then enlarged and

projected on a Richardson 3600 lines/mm grating for a frequency correlated angular span,

and the angular span is converted into a spacial span by a 1m long propagation.

Eventually, the useful signal is selected by a slit and sent into a photodiode. The setup is

shown in Fig. 3.22.
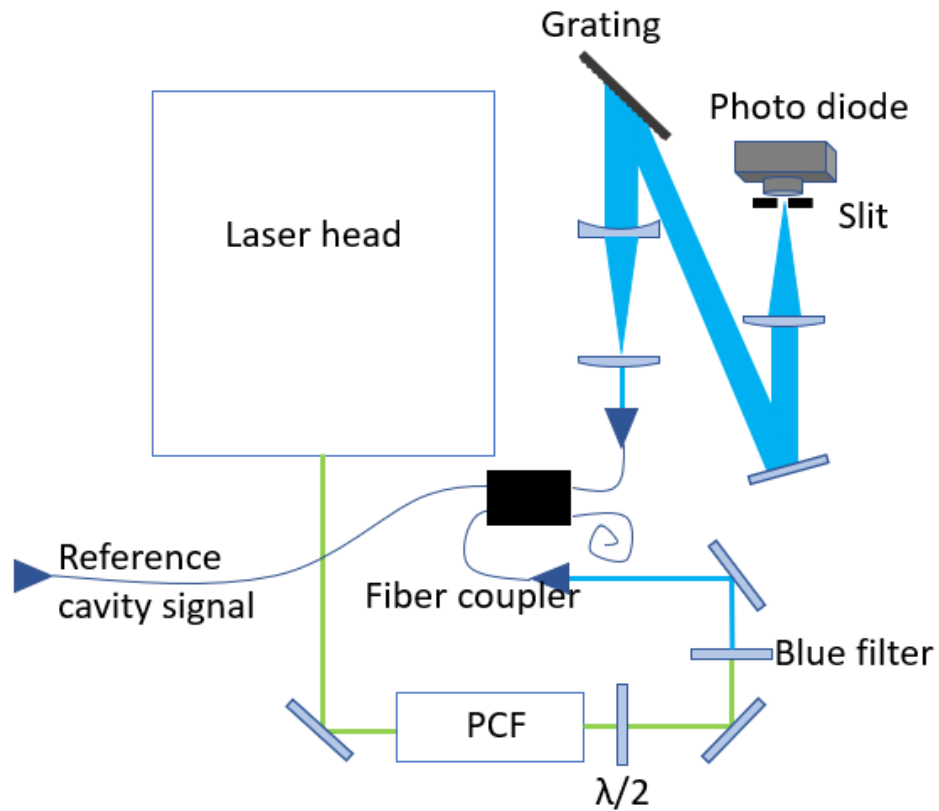
Figure 3.22 Frequency comb optics setup.

When performing frequency metrology, the CEO is locked at ±60MHz while the repetition rate is fixed at around 250MHz. The repetition value could either be locked to a preset value or a value that fixes the beating frequency to ±60 MHz. The former method is called RF locking, and the latter one is called optical locking. We choose the second approach as it provides better uncertainty in frequency metrology. After an upgrade of locking electronics from Menlo, the optical locking could be achieved with a 10dB SNR on the beating signal at a Hz-scale Allen variance. The beating SNR could normally be tuned to 15dB.

While the f_{rep}, the f_{ceo}, and the f_{beat} can be measured to sub-Hz scale by the FX80E counter installed on the comb control. The integer N, approximately 2.5 million, must be specified to the correct integer to calculate the reference signal frequency. Here we present an algorithm eliminating any error in the calculation of N.

To specify N, we have to perform optical lockings at two different f_{rep}, and for convenience, we assume the f_{ceo} and f_{beat} to be the same for these two cases, which can be easily set by the comb control hardware and software. Thus the two measurements satisfy equation 3.9.

$$f_{ref} = N_1 f_{rep_1} + f_{ceo} + f_{beat} = N_2 f_{rep_2} + f_{ceo} + f_{beat}$$

$$N_1 f_{rep_1} = N_2 f_{rep_2}$$

Equation 3.9

Assume $N_1 > N_2$ and $f_{rep1} < f_{rep2}$, the second equation in 3.9 can be converted to equation 3.10.

$$(N_2 + \Delta N) f_{rep_1} = N_2 \left(f_{rep_1} + \Delta f \right)$$

$$N_2 = \frac{\Delta N \ f_{rep_1}}{\Delta f}$$

Equation 3.10

From equation 3.10, we can see that the determination of N_2 relies on the uncertainty of f_{rep1} and Δf. To reduce the uncertainty, the two measurements are made at two repetition rates separated as far as allowed by the apparatus, which are around 250.25 MHz and 249.75 MHz.

Another factor in determining N_2 is to find the exact value of ΔN. As both N_2 and ΔN are integers, we could use a "trial frequency" to find the approximate ΔN and use integer values near the trial ΔN to see which integer gives an integer N_2. However, a caveat has to be mentioned regarding this approach. Say the two rep-rate values are 250.25MHz and 249.75MHz, which gives a $\Delta f = 0.5$ MHz. An integer estimation of N_2 will show up with every increment by 2 in ΔN. To further reduce a possible erroneous ΔN, we inserted two checkpoints at $f_{rep3} = f_{rep1} + \Delta f /7$ and $f_{rep4} = f_{rep1} + \Delta f /9$. Then the adjacent $\Delta N'$ giving integer N_2, N_3, and N_4 can only be found at $\Delta N + LCM(2, 7, 9)$, 126 orders away from the correct value. Thus a correct ΔN could easily be identified as the next arithmetically correct order would lead to a frequency too far away to be physically valid.

Although the reference possesses excellent thermal stability, the resonance could still drift when locked due to the laser power. If the measurement is conducted within 10min, the drift would be less than 50kHz and is unlikely to produce any error in frequency calculation. If measurement experiences a longer time, notice to the drift has to be made to reduce potential error in the calculation.

3.6   Reference Clock

We use an EndRun Meridian II Precision TimeBase clock to produce 10MHz RF reference signals for all devices requiring a clock, including the frequency comb, all oscilloscopes, and AOM drivers. This GPS-based clocked has a temperature control system providing thermal stability of 0.5 ppb, and the phase noise is -113 dBc/Hz. The Allan Deviation of the clock phase regarding testing interval is presented in Fig. 3.23 [22].
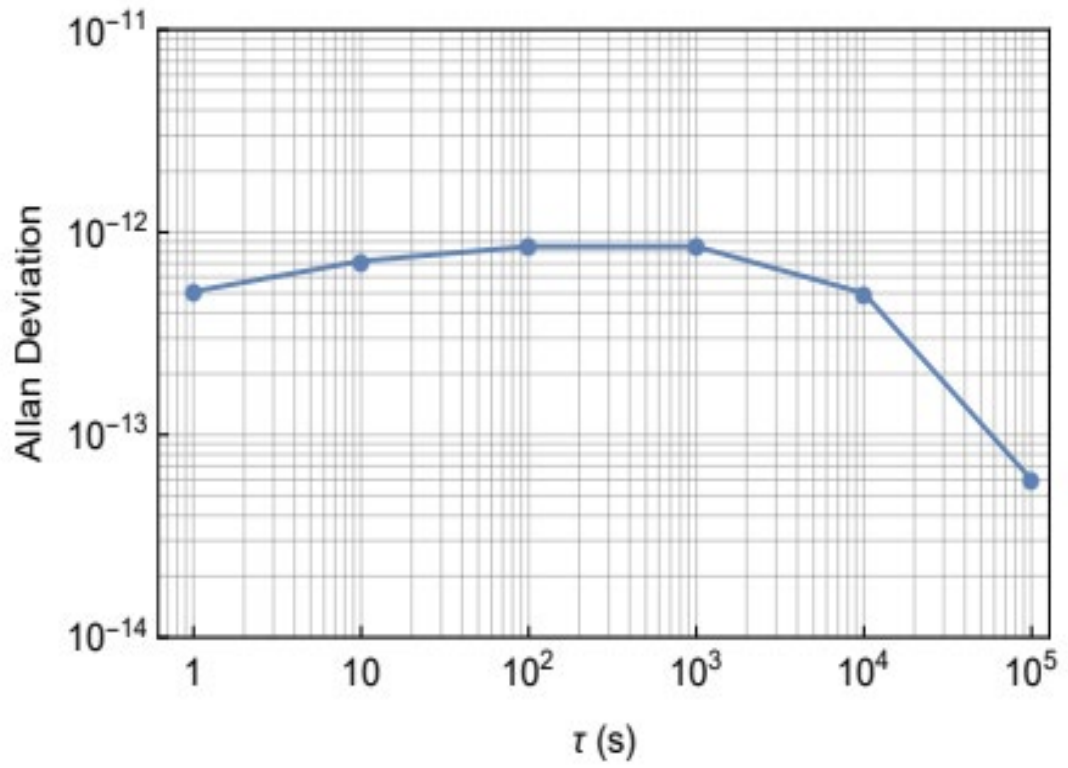
Figure 3.23 GPS clock's phase's Allan deviation vs. testing time.

Chapter 4

1S-2P experiment

4.1 Pulsed Lasers

We use a Surelite SLIII-10 Nd: YAG laser as the source of our pulsed laser system. The Nd: YAG laser generates 2Hz 1200mJ 6ns pulses at 1064nm, which is later frequency-doubled and frequency-tripled to about 90mJ of 532nm and 270mJ of 355nm before emitting out of the chassis. Another SHG crystal is set out of the chassis to further convert the residual 1064nm power to about 90mJ of 532nm.

The 532nm and 355nm lasers are sent into two Quanta Ray PDL-1 dye lasers generating 734nm and 486nm pulses, respectively. Each dye laser has three stages: oscillator, pre-amplifier, and a terminating amplifier. The first two stages of both dye lasers and the last amplifier of the 486nm laser are side-pumped, while the last stage for the 734nm dye laser is in-line pumped. And a 10mJ 486nm pulse and an 8mJ 734nm pulse are generated at a 2Hz rate. The 486nm pulses are sent into an SHG crystal, generating 1mJ 243nm pulses. These two pulses are overlapped on the optical table and sent to the UHV chamber through a light pipe, preventing potential hazards from stray light.

The frequencies of these pulsed lasers are measured by a Bristol wavemeter. The wavemeter is calibrated with a HeNe laser with an in-air wavelength at 632.8nm with

0.01 nm precision. A reproducible reading offset of +13.75 GHz at 486 nm is detected on the wavemeter. We will use the wavemeter reading to identify the pulsed laser frequency or wavelength in the following content of this section, which may be slightly off from the actual wavelength or frequency.

4.2   1S-2P Experiment

The temporally and spatially overlapped 243 nm and 734 nm pulses transmit through the excitation chamber vertically, skimming the Ps sample. The UV saturation of the MCP detector can be used to adjust the laser spot's distance to the sample. Then a beam blocker is laid on the top window, trimming off a portion on the edge of the spot that causes the UV scattering. About four-fifths of the laser spot is projected in front of the sample in the Ps trajectory toward the MCP plate.

As the pulsed laser is projected vertically and the Ps atoms transport to MCP horizontally, the Doppler broadening is only on at GHz scale and is covered by the frequency span of the pulsed laser. So the excitation of a Ps atom is not limited by the Doppler shift as long as it shows up in the laser spot.

With alignment setup, three degrees of freedom were scanned: 243 nm laser frequency, 734 nm laser wavelength, and the delay time between the e^+ and laser pulse. The Rydberg Ps counting peaks show up at UV laser $f \sim 1\,233\,690$ GHz, IR laser $\lambda \sim$ 733.75 nm, and 734.28 nm. According to the interval between these two wavelengths, the two peaks on the IR spectrum indicate Rydberg states of $n = 25$ and $n = 24$.
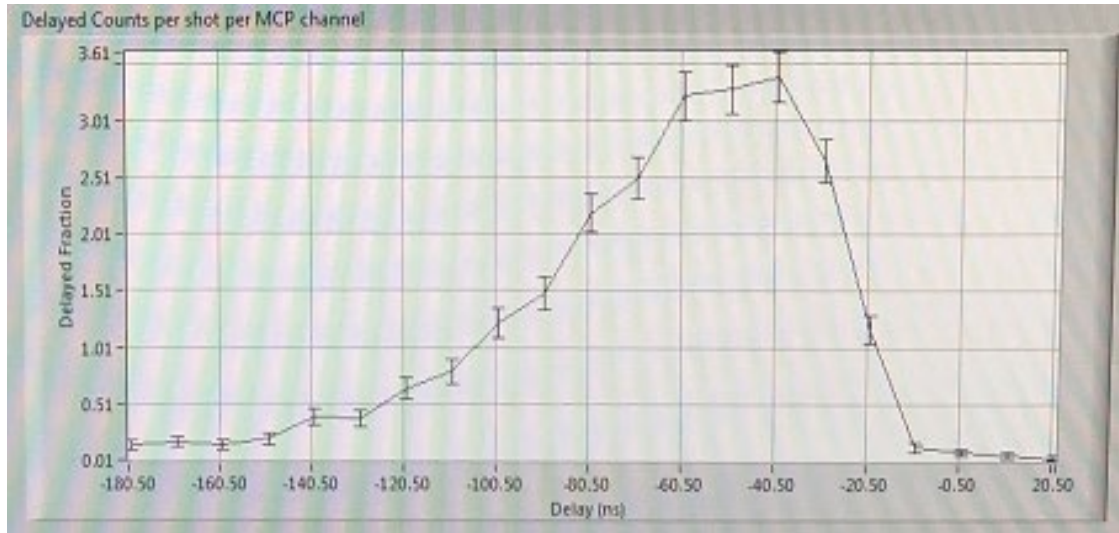
Figure 4.1 Counts per event vs. delay time.

Fig 4.1 is an example curve of the Rydberg Ps counts per event collected by the MCP detector vs. the delay time. The horizontal axis in Fig. 4.1 is the delay time $t_d = t_e - t_o$, a value defined by the e^+ pulse firing trigger t_e minus the laser pulses firing trigger t_o. It is different from the actual delay time between e^+ and laser pulses by a constant. This constant needs to be determined in future experiments. The laser spot is 8mm in size, and the center is about 4mm away from the sample surface.

From Fig. 4.1, we can see that the arrival time of the laser pulses relative to the e^+ pulse can affect the count rate of excited Ps. Note that the laser spot is about 8mm in diameter, and the duration is about 5ns, so even with a specified delay time, the excited Ps atoms could possess a range of velocities due to the specific excitation location and time in the laser spot. For example, if the laser spot's distance from the sample is from x_1 to x_2, where $x_2 - x_1 = 8$mm, and the laser arrival time relative to the Ps emission time is t_1 to t_2, where $t_2 - t_1 = 5$ns, then the velocity of excited Ps atoms can range from x_1/t_2 to $x_2/$

62

t_1. In the experiment of Fig. 4.1, the laser spot is set at a fixed distance $(x_1 + x_2)/2 = 4$mm, from the sample. So shifting the delay time $t_d = t_1 + c$, where c is a constant, will change the velocity range of the excited Ps atoms, thus the count rate of Ps atoms because of the Boltzmann distribution of Ps velocities. However, this figure only shows a qualitative property of the Ps atom velocity distribution. For the quantitative properties, further experiments with better information of Ps velocities need to be performed, and parameters of the distribution need to be decided by curve fitting.

If the laser spot changes its location, the count vs. delay-time curve will change too. We performed another experiment with the laser spot center set 10mm away from the sample surface. The maximum count drops to 0.5count/event and shifts to $t_d = 100$ns, indicating that the Ps atoms at the most probable velocity arrive later at the laser spot with a drop in population due to annihilation.

Fig 4.1 also demonstrates a 3.61 maximum count rate that is seven times better than a previous experiment in 2018, and the best count rate we recorded was 4.4 counts per event. The improvement comes from a new e^+ source, better laser intensity, and laser alignment. However, we estimated 110 Ps atoms flying towards the MCP for each e^+ event but only recorded less than 5 of them. Several factors may contribute to the loss. (1) To avoid intervention between the MCP frame and the interferometer frame, we have to retract the MCP a little bit, and a portion of the MCP surface is blocked by the UHV chamber wall. (2) Limited by the spatial spot and temporal duration of the laser pulse, only part of the Ps atoms can be excited, and (3) due to the 142ns lifetime, there is a

chance Ps atoms may annihilate before being excited. The details of these factors need to be studied more carefully in the future.

We also analyzed the raw data recorded by the MCP, as shown in Fig. 4.2. The bottom graph of Fig. 4.2 shows all the counts recorded by the MCP detector in the same experiment as in Fig. 4.1. The horizontal axis is the arrival time relative to the e^+ firing trigger, and the vertical axis is the accumulated counts at different arrival-time intervals. In Fig. 4.2, the counts detected at all delay time t_d on Fig. 4.1 horizontal axis are accumulated.

Although the trajectory of each Ps atom is not known precisely, and the ToF can only be roughly known with about 30ns uncertainty due to the time a Ps can spend in the pores of the sample, we still estimated the velocity distribution. In the estimation, we used 30cm as the trajectory length for all atoms, and ToFs are estimated by arrival time minus Gamma radiation peak minus 30ns spent in sample pores. The estimation of velocity distribution is demonstrated in Fig. 4.2 top. The horizontal axis is the estimated velocities, and the vertical axis is the percentage of Ps atoms normalized by the number in each velocity interval divided by total number counts 7560. The arrival time shows a peak at about 3300ns after the trigger, and the estimated most probable velocity is about 1×10^5m/s, with an FWHM of about 5×10^4m/s.

By estimating the velocity distribution of Ps atoms using the $1S$-$2P$ experiment, we can estimate the second-order Doppler shift in the $1S$-$2S$ experiment and how much we need to detune the CW laser frequency.
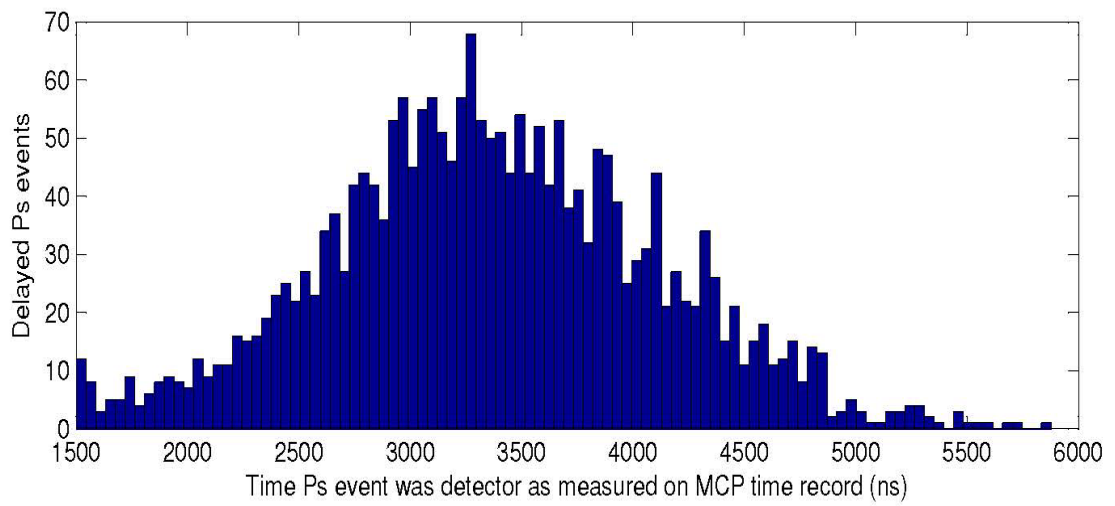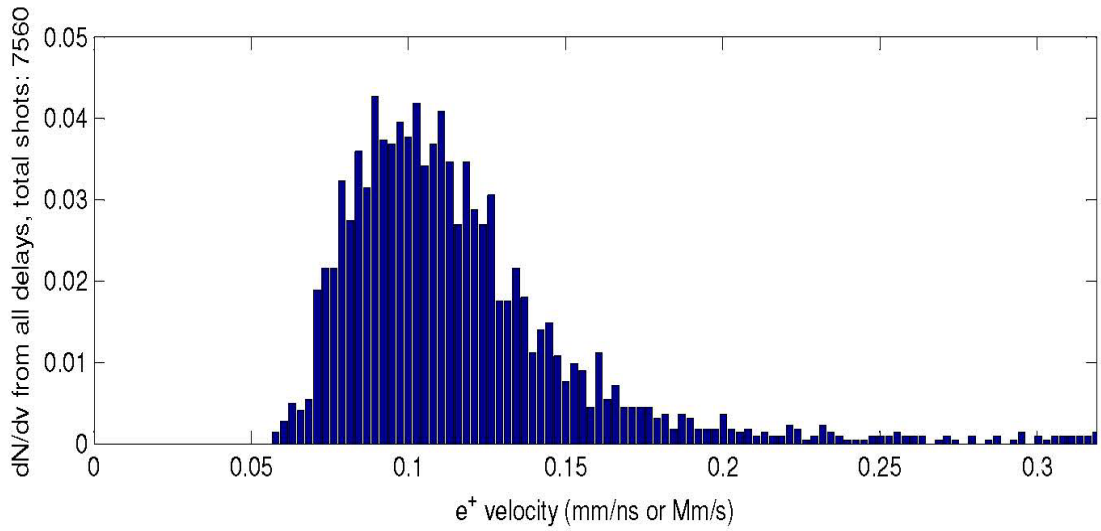
Figure 4.2 Ps velocity and MCP counts distribution

Chapter 5

1S-2S experiment design and data collection

5.1 Shifts and Broadening

The natural linewidth of the Ps 1^3S_1-2^3S_1 interval is mainly determined by the annihilation lifetime, as shown in equation 5.1. The 142ns is the lifetime of the 1S triplet state, and the 1.136μs is the 2S triplet state annihilation lifetime which is 142ns scaled by a factor 8, the cube of the principal quantum number. In contrast, the 2-photon transition contribution is trivial. Thus the natural linewidth is 1.261 MHz and provides an ideal source for ultrafine spectroscopy compared with other intervals [84].

$$\frac{1}{T} = \frac{1}{142ns} + \frac{1}{1.136\mu s} = \frac{1}{126.2ns}$$

$$\delta v = \frac{1}{2\pi T} = 1.261 \; MHz$$

Equation 5.1

The natural linewidth can be broadened or shifted as a result of Doppler shift, Stark shift, and transit-time broadening. We will talk about the contribution of each of these terms below.

The Doppler broadening is an inhomogeneous process in which the shift depends on the velocity of each particle. Fortunately, the odd-order Doppler shifts disappear in the two-photon excitation process involving two counter-propagating beams at precisely the

same frequency, which is the case in the interferometer. However, we still need to consider the second-order Dopper shift, which motivates us to record the individual trajectory of each particle in our experiment.

The second-order Doppler shift is determined by equation 5.2, where $\delta\nu_D$ is the 2nd order Doppler shift, and $\nu_0 = 1\,233\,607\,216.4$ MHz is the Ps 1^3S_1-2^3S_1 interval. Based on the histogram in section 4.2, the Ps atoms have a Doppler broadening spectrum centered at -70MHz, and the half-maximum spans approximately from -40MHz to -100MHz.

$$\delta\nu_D = -\frac{1}{2}\left(\frac{v}{c}\right)^2 \nu_0$$

Equation 5.2

The Stark shifts include the DC stark shift, the AC Stark shift, and the motional Stark shift. The chamber walls and sample stick are all grounded to avoid DC electric fields caused by charge accumulation. Magnetic fields from the e^+ beamline are also insulated by μ-metal, but the 47μT earth field around our lab may cause a motional Stark shift at about 360 kHz. Due to the oscillating electric field, the AC Stark shift has to be taken into consideration. The AC Stark shift is determined by equation 5.3.

$$\delta\nu_{AC} = 13.3\frac{cm^2}{J} \times I\frac{W}{cm^2}$$

Equation 5.3

The beam profile can be precisely determined, as demonstrated in chapter 3. Despite a higher power compared with Fee et al.'s apparatus [39], the larger beam size

will reduce the AC Stark shift by approximately a factor of 2. Moreover, with the trajectory of Ps atoms, the AC stark shift for each particle can be calculated.

Transit time broadening also needs to be considered due to the Uncertainty Principle. The time a particle spends interacting with the electric field affects the accuracy of its line. Equation 5.4 shows the effect of interaction time. The τ_n is the natural lifetime, and the τ_t is the transit time [85].

$$\delta v_t = \frac{1}{2\pi}\left(\frac{0.5346}{\tau_n} + \sqrt{\frac{0.2166}{\tau_n{}^2} + \frac{22.18}{\tau_t{}^2}}\right)$$

Equation 5.4

In our experiment design, the transit time is extended by a large beam size ($\omega = 0.942$nm) and a large tilting angle ($80°$) of the Ps trajectory. The transit time can be calculated by equation 5.5, and the broadening is approximately 7MHz, as opposed to ten-times wider broadening if Ps atoms cross the beam straightly. Luckily, transit time broadening is symmetric, so curve fitting upon a large amount of data can locate the center of transit time broadening to kHz precision.

$$\tau_t = \frac{2\omega}{\cos(80°)\ v_{Ps}} \approx 110ns$$

Equation 5.5

5.2   Experiment Design

Like in the 1S-2P experiment, many alignments and parameters have to be adjusted such that the Ps can be successfully excited to the 2S and Rydberg states and be recorded. We will talk about the experiment design in this section.

5.2.1 Spatial alignment
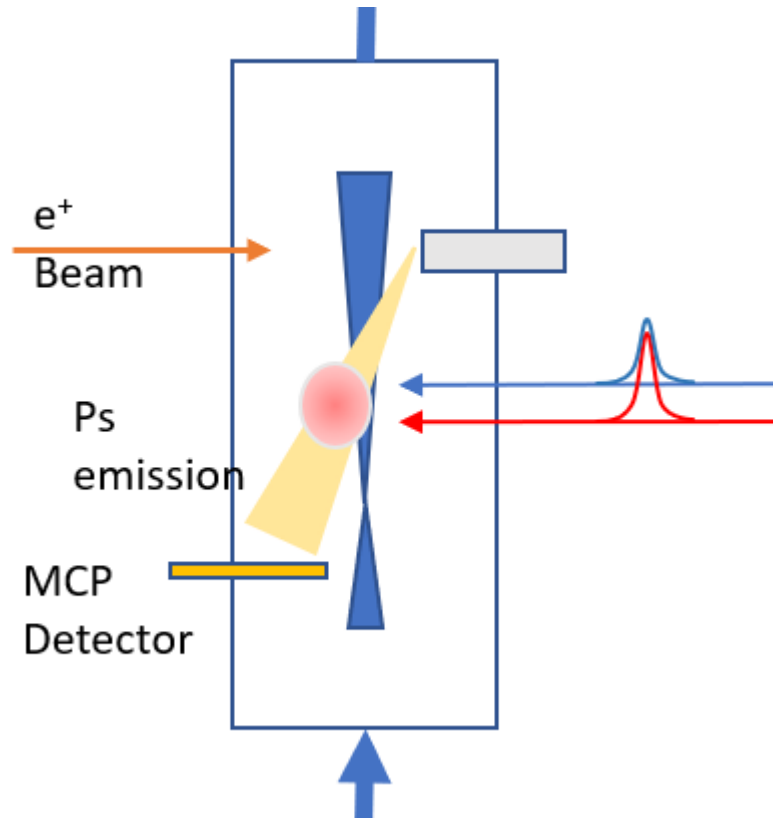
Figure 5.1 Schematic view of the spatial alignment of lasers.

In the 1S-2P alignment, the pulsed laser spot can be set close to the sample for maximum yield. However, in the 1S-2S experiment, the excitation region is defined by the CW laser profile and the Ps trajectories. The pulsed laser spot has to be set slight after the 1S-2S excitation region along the Ps trajectories to excite 2S Ps to Rydberg states while avoiding the AC stark shift induced by the strong field of the pulsed laser. Otherwise, the 2S Ps atoms may only travel for about 10cm if not excited to Rydberg states and cannot reach the MCP detector.

5.2.2   Delay time

In the 1S-2P excitation, the pulsed lasers can span to several GHz on the frequency domain, covering even the Doppler broadened spectrum as the vertical velocity distribution of Ps atoms is small. Adjusting the delay time can help select the group of Ps atoms with a certain range of velocities.

Nevertheless, in the 1S-2S experiment, the CW laser only has a linewidth of several kHz. As a result, only a small portion of Ps atoms, whose velocity can shift their line to the MHz vicinity of the CW laser, can be excited. The MHz vicinity results from the 1.26MHz natural linewidth and 7MHz transit time broadening. In contrast, the Doppler shift due to velocity distribution extends to a range > 100MHz. Once the CW laser frequency is fixed, the velocity distribution of the able-to-be-excited Ps atoms is limited to a small range, and their arrival time into the excitation region is determined. The delay time has to be set so that the 734nm pulses simultaneously arrive at the excitation region with candidate Ps atoms.

As the first step, we want to record any Ps 1S-2S count regardless of their speed. So the best approach is to select the velocity group with the largest possibility density. Fortunately, the 1S-2P experiment can help analyze the velocity distribution of the Ps atoms, as shown in chapter 4. Based on the velocity distribution and the excitation region geometry, we calculated the most populated Ps velocity group arrives at the excitation regions at about 100ns after the e^+ pulse. So using the 1S-2P experiment, we translate the 243/734nm laser spot toward the MCP plate until the peak of counts shows up at 100ns

delay time. Then we set the CW laser frequency to a reasonable value determined by the 1S-2S interval and shifts, and data are accumulated for hours.

5.2.3 Pulsed IR laser frequency

The 2S-Rydberg transition frequency is slightly different from the 2P-Rydberg value, so we need to detune the 734nm pulsed laser frequency for the 2S-Rydberg transition.

For the linearly polarized 243nm pulsed laser we use in our 1S-2P experiment, the 1S triplet states may be excited to 8 possible 2P states:

2P states	m
2^3P_0	0
2^3P_1	-1, 0, 1
2^3P_2	-1, 0, 1

Table 5.1 Possible 2P states excited by 243nm linearly polarized laser.

These states lie on two distinct energy levels labeled -980MHz and -5365MHz in [21], while the 1S triplet state is marked at 7647MHz. So the 734nm pulsed laser needs to be redshifted by 10819MHz.

$$7647MHz - (-980MHz - 5364MHz)/2 = 10819MHz$$

Equation 5.6

5.2.4 CW laser frequency

Due to the second-order Doppler shift calculated above, the frequency seen by the atom is red-shifted from the laser frequency. So we need to detune the laser frequency to the blue side to compensate for this value. For example, for the most probable velocity at

1×10^5m/s, the total shift from the 1S-2S interval is about 70MHz. We use the 486nm laser for two-photon excitation, so the 486nm CW laser needs to be blue-shifted by about 35MHz. We found one reference cavity resonance at approximately 190MHz above the theoretical value of Ps 1S-2S interval with frequency comb measurement. So the AOM system should set the interferometer frequency at about 155MHz below the reference cavity resonance. In other words, AOMs should up-shift the interferometer frequency by 155MHz and lock to the ULE cavity.

5.3   1S-2S Transition Count Rate and S/N ratio optimization

We achieved at best 4.4 Rydberg Ps counts per shot collected by the multiple channel plate in $1S$-$2P$ experiments. However, $1S$-$2S$ transitions rates are much lower. The two-photon absorption process required by $1S$-$2S$ transition has a much smaller cross-section than the single-photon $1S$-$2P$ transition.

As to the laser intensity and quantum yield, the instant intensity of the CW laser, which is at 5 kW, is orders of magnitude lower than the 1mJ 5ns duration UV pulsed laser. However, the quantum yield scales with $(E^2t)^2$ in the small-signal limit, where E is the electric field and t is the time an atom spends in the field. As opposed to the 5ns pulsed laser, a Ps atom can spend as long as 142ns lifetime in the CW laser beam, equivalent to a 0.7mJ laser pulse. So we expect a drop in yield due to the laser intensity, but the drop is less than an order of magnitude. We can estimate it to be a factor of 0.5.

Moreover, the CW laser has a sharp linewidth, but due to the transit time broadening and natural linewidth, Ps transition frequency can be broadened to 7MHz. However, the second-order Doppler shift due to Ps atom velocity distribution extends

from -40MHz to -100MHz. And the 7MHz broadening could only cover about 10% of Ps atom velocities. Considering the quantum yield, we estimate that only about 5% of Ps atoms are likely to be excited compared with the $1S$-$2P$ experiment, so we are expecting a count rate of 0.15ct/event.

There are several strategies to increase the S/N ratio. First, the noise counts on MCP have to be reduced. The noise counts may come from dark counts, the environment, the laser signals, and the e^+ pulses. Recent experiments show that the last factor may be the largest contribution. To reduce the counting of noise, we can limit the time window on the MCP oscilloscope and the spatial region on the MCP plate.

Since the velocity distribution of the 2S excited Ps atoms is well defined, the excited Rydberg atoms will arrive at the MCP within a tiny time window. For example, if the velocity group is centered at 1×10^5m/s, 7MHz broadening results in a velocity distribution from 9.75×10^4m/s to 1.025×10^5m/s, thus the travel time to the MCP 30cm away will be from 2926ns to 3076ns. Considering the 30ns delay-time a Ps may spend in the sample and the travel length difference varied by each trajectory, we only need to count a window at 3000ns±100ns. As we are most interested in the Ps atoms that spend long enough in the laser beam, we can take advantage of the spatial resolution of the MCP plate and only record the region close to the laser beam, so the noise counts elsewhere can be abandoned.

Dark counts on the MCP can be reduced by applying HV on MCP for more than 24hr, allowing the ionized particles to be released from the porous on the MCP.

Second, signals of Ps 1S-2S transition counts need to be improved. Extra efforts in alignments are also necessary to guarantee the Ps atoms can be properly excited. If necessary, we plan to apply the lock-in amplifying technique. We can modulate one factor and make the Ps 1S-2S transition happen at 1Hz and allow the rest of the factors to happen still at 2Hz. By multiplying the total signal with a 1Hz wave in phase, noise counts will be averaged towards zero while 1S-2S counts are amplified.

5.4 Uncertainties and Data Analysis

5.4.1 Reference frequency

The reference cavity has a linewidth of <50kHz, specified by the manufacturer Stable Laser Systems, Inc. However, the frequency measured by the frequency comb counter has an oscillation with an amplitude of 50kHz at 60Hz frequency. This 60Hz frequency appears at all counter channels, so it is most likely a ground loop noise generated by the comb electronics. It can be averaged out by averaging the frequency counting to 1s, then the uncertainty on the reference frequency can be suppressed to <50kHz/60 = 0.83kHz.

5.4.2 Instantaneous frequency

After all the noise suppression effort, the resonance oscillation amplitude (half of the peak-peak value) is 60kHz, and the acoustic noise frequency up limit is 1000Hz. Consider a single-mode acoustic noise at 1000Hz. The resonance oscillation can be expressed by equation 5.7.

$$\delta f(t) = 60kHz \times \sin{(2\pi 1000Hz \times t)}$$

Equation 5.7

74

We record a 100μs time window before excitation with the oscilloscope, and the excitation time can be easily located to a range within 10μs or even smaller. With the maximum 20GS/s sampling rate of the oscilloscope, the time of each sample data can be resolved to 50ps. And the beating frequency, which is at most 190MHz (see section 5.2.4), can be resolved to less than 1kHz.

Another approach to precisely measure the instantaneous frequency is to use a polynomial function ($f_0 + f_1 t + f_2 t^2 + f_3 t^3$) to replace the frequency f of the beating signal and normalize the amplitude using $\sqrt{I_{int} \times I_{ref}}$, where I_{int} is the intensity of the interferometer and I_{ref} is the intensity of the reference cavity.

5.4.3 AC Stark shift

The AC Stark shift is determined by the laser intensity experienced by the Ps atoms. To know the AC Stark shift for each atom, we have to know (1) circulating laser power (2) laser profile (3) Ps trajectory in the laser beam. The laser profile can be determined with great precision, as described in Chapter 3, and the Ps trajectory can be given by MCP. However, it is challenging to determine the circulating laser power. Although with the assumption $t_1 = t_2$ and $l_1 = l_2$ (see section 3.2), we can estimate the circulating power. To precisely calculate the circulating power, we have to know the individual transmission coefficient for each mirror. Thus an experiment measuring these coefficients is required in the future.

5.4.4 Second-order Doppler shift

Doppler shift is proportional to the velocity squared, as shown in Eq. 5.2. So if we can measure the transition frequency δv_d and velocity v of each excited Ps atom, we can fit the curve of δv_d vs. v.

On the vertical axis of δv_d vs. v, there will be around 7MHz uncertainty due to transit time broadening and natural linewidth. By increasing the number of data points, this uncertainty can be suppressed statistically.

The velocity is calculated by the trajectory length divided by ToF $v = L/t$. In the measurement of trajectory length, there will be an ± 1mm absolute error due to the measurement of dimensions in the chamber or the MCP resolution. It will generate an uncertainty of ± 1mm/30cm $= \pm 0.3\%$ in L or v, or 0.6% uncertainty in δv_d because of the second-order dependence on velocity.

As for the time measurement, we have to consider the emission time of Ps atoms from the sample. Although the Ps emission can take 25ns~30ns which is relatively long considering the ToF is about 3000ns, if we can determine the centroid of the Ps emission and set it as t_0, which means half of Ps atoms are emitted before this point and the other half after this point, we can make the uncertainty on the emission time a random error and be suppressed by statistical method. For example, if the emission time generates a $\pm 0.5\%$ error (± 15ns/3000ns), with 100 data points, the fitting can average this error to about 0.05%. However, there could also be absolute errors in time measuring as the time is recorded on a nanosecond scale, so the hardware needs to be examined carefully to reduce the absolute error in time measuring.

Using slower positronium with longer ToF can also reduce the error bar on velocity measurement, but slower Ps atoms have a lower yield, which increases the difficulty in data collection.

Chapter 6

Conclusion

We have made significant progress in the Ps $1S$-$2S$ spectroscopy, demonstrated by the considerable performance improvement of the apparatus and the yield improvement of the $1S$-$2P$ experiment. We are also planning a Ps $1S$-$2P$ precision spectroscopy experiment with the current setup and a narrow linewidth dye laser, which has been purchased from Germany.

Ps $1S$-$2S$ spectroscopy is being performed, and efforts are spent on improving the S/N ratio of the MCP signal. Trajectory analysis tools are also prepared for precise in situ dimension measurement. In the near future, we expect to achieve kHz scale Ps 1S-2S spectroscopy data, which hopefully can shed light upon the unsolved puzzles in fundamental physics.

Bibliography

1.	Dirac, P.A.M.J.P.o.t.R.S.o.L.S.A., Containing Papers of a Mathematical and P. Character, *The quantum theory of the electron.* 1928. **117**(778): p. 610-624.

2.	Dirac, P.A.M.J.P.o.t.R.S.o.L.S.A., Containing papers of a mathematical and p. character, *A theory of electrons and protons.* 1930. **126**(801): p. 360-365.

3.	Dirac, P.A.M.J.P.R.S.L.A.S., *Quantised singularities in the quantum field.* 1931. **1**: p. 133.

4.	Anderson, C.D.J.P.R., *The positive electron.* 1933. **43**(6): p. 491.

5.	Mohorovicic, S.J.A.N., *Möglichkeit neuer Elemente und ihre Bedeutung für die Astrophysik.* 1934. **253**: p. 93.

6.	Deutsch, M.J.P.R., *Evidence for the formation of positronium in gases.* 1951. **82**(3): p. 455.

7.	Mills, A.P. and S. Chu, *Excitation of the Positronium 1 3 S 1-2 3 S 1 Two Photon Transition*, in *Atomic Physics 8*. 1983, Springer. p. 83-101.

8.	Usukura, J., K. Varga, and Y.J.P.R.A. Suzuki, *Signature of the existence of the positronium molecule.* 1998. **58**(3): p. 1918.

9.	Cassidy, D.B. and A.J.N. Mills, *The production of molecular positronium.* 2007. **449**(7159): p. 195-197.

10.	Alonso, A., et al., *Controlling positronium annihilation with electric fields.* 2015. **115**(18): p. 183401.

11.	Bethe, H.A. and E.E. Salpeter, *Quantum mechanics of one-and two-electron atoms.* 2012: Springer Science & Business Media.

12.	Alekseev, A.J.Z.E.i.T.F., *Two-photon annihilation of positronium in the P-state.* 1958. **34**.

13.	Alekseev, A.J.S.P.J., *Three-photon annihilation of positronium in the P-state.* 1959. **9**: p. 1312.

14.	Breit, G. and E.J.T.A.J. Teller, *Metastability of Hydrogen and Helium Levels.* 1940. **91**: p. 215.

15. Karshenboim, S.G.J.I.J.o.M.P.A., *Precision study of positronium: Testing bound state QED theory.* 2004. **19**(23): p. 3879-3896.

16. Badertscher, A., et al., *Improved limit on invisible decays of positronium.* 2007. **75**(3): p. 032004.

17. Cooke, D., et al., *Observation of positronium annihilation in the 2S state: towards a new measurement of the 1S-2S transition frequency.* 2015. **233**(1): p. 67-73.

18. Ley, R., et al., *Spectroscopy of excited state positronium.* 1994. **89**(1): p. 327-341.

19. Bernreuther, W., O.J.Z.f.P.C.P. Nachtmann, and Fields, *Weak interaction effects in positronium.* 1981. **11**(3): p. 235-245.

20. Govaerts, J. and M.J.P.L.B. Van Caillie, *Neutrino decay of positronium in the Standard Model and beyond.* 1996. **381**(4): p. 451-457.

21. Gurung, L., et al., *Precision microwave spectroscopy of the positronium n = 2 fine structure.* 2020. **125**(7): p. 073002.

22. Goldman, H.J., *Apparatus for Ultrahigh Precision Measurement of 1 3 S 1–2 3 S 1 Interval in Positronium.* 2018: University of California, Riverside.

23. Pachucki, K. and S.G.J.P.r.l. Karshenboim, *Complete Results for Positronium Energy Levels at Order m α 6.* 1998. **80**(10): p. 2101.

24. Czarnecki, A., K. Melnikov, and A.J.P.R.A. Yelkhovsky, *Positronium S-state spectrum: Analytic results at O (m α 6).* 1999. **59**(6): p. 4316.

25. Czarnecki, A., K. Melnikov, and A.J.P.r.l. Yelkhovsky, *Positronium Hyperfine Splitting: Analytical Value at O (m α 6).* 1999. **82**(2): p. 311.

26. Adkins, G.S., R.N. Fell, and P.M.J.P.R.A. Mitrikov, *Calculation of the positronium hyperfine interval using the Bethe-Salpeter formalism.* 2002. **65**(4): p. 042103.

27. Adkins, G.S., R.N. Fell, and J.J.A.o.P. Sapirstein, *Two-loop correction to the orthopositronium decay rate.* 2002. **295**(2): p. 136-193.

28. Zatorski, J.J.P.R.A., *O (m α 6) corrections to energy levels of positronium with nonvanishing orbital angular momentum.* 2008. **78**(3): p. 032103.

29. Pachucki, K. and S.G.J.P.R.A. Karshenboim, *Higher-order recoil corrections to energy levels of two-body systems.* 1999. **60**(4): p. 2792.

30. Kniehl, B.A. and A.A.J.P.r.l. Penin, *Order α 7 ln (1/α) contribution to positronium hyperfine splitting*. 2000. **85**(24): p. 5094.

31. Melnikov, K. and A.J.P.r.l. Yelkhovsky, *O (α 3 ln α) Corrections to muonium and positronium hyperfine splitting*. 2001. **86**(8): p. 1498.

32. Baker, M., et al., *Hyperfine Splitting in Positronium to O (α 7 m e): One Photon Annihilation Contribution*. 2014. **112**(12): p. 120407.

33. Adkins, G.S., et al., *Three-photon-annihilation contributions to positronium energies at order m α 7*. 2015. **115**(23): p. 233401.

34. Adkins, G.S., L.M. Tran, and R.J.P.R.A. Wang, *Positronium energy levels at order m α 7: product contributions in the two-photon-annihilation channel*. 2016. **93**(5): p. 052511.

35. Adkins, G. *Higher order corrections to positronium energy levels*. in *Journal of Physics: Conference Series*. 2018. IOP Publishing.

36. Eides, M.I. and V.A.J.P.R.D. Shelyuto, *One more hard three-loop correction to parapositronium energy levels*. 2017. **96**(1): p. 011301.

37. Tiesinga, E., et al., *CODATA recommended values of the fundamental physical constants: 2018*. 2021. **93**(2): p. 025010.

38. Mohr, P.J., et al., *CODATA recommended values of the fundamental physical constants: 2014*. 2016. **45**(4): p. 043102.

39. Fee, M.S., et al., *Measurement of the positronium 1 (3)S1-2 (3)S1 interval by continuous-wave two-photon excitation*. Phys Rev A, 1993. **48**(1): p. 192-219.

40. Mohr, P.J., et al., *CODATA recommended values of the fundamental physical constants: 2006*. 2008. **80**(3): p. 633-1284.

41. Mohr, P.J., B.N. Taylor, and D.B. Newell, *CODATA recommended values of the fundamental physical constants: 2010*. 2012.

42. Pohl, R., et al., *The size of the proton*. Nature, 2010. **466**(7303): p. 213-6.

43. Antognini, A., et al., *Proton structure from the measurement of 2S-2P transition frequencies of muonic hydrogen*. 2013. **339**(6118): p. 417-420.

44. Beyer, A., et al., *The Rydberg constant and proton size from atomic hydrogen*. 2017. **358**(6359): p. 79-85.

45. Fleurbaey, H., et al., *New measurement of the 1 S− 3 S transition frequency of hydrogen: contribution to the proton charge radius puzzle.* 2018. **120**(18): p. 183001.

46. Xiong, W., et al., *A small proton charge radius from an electron–proton scattering experiment.* 2019. **575**(7781): p. 147-150.

47. Mihovilovič, M., et al., *The proton charge radius extracted from the initial-state radiation experiment at MAMI.* 2021. **57**(3): p. 1-9.

48. Hayward, T.B. and K.A.J.N.P.A. Griffioen, *Evaluation of low-Q2 fits to ep and ed elastic scattering data.* 2020. **999**: p. 121767.

49. Onofrio, R.J.E., *Proton radius puzzle and quantum gravity at the Fermi scale.* 2013. **104**(2): p. 20002.

50. Dahia, F. and A.J.T.E.P.J.C. Lemos, *Is the proton radius puzzle evidence of extra dimensions?* 2016. **76**(8): p. 1-7.

51. Liu, Y.-S., D. McKeen, and G.A.J.P.r.l. Miller, *Electrophobic scalar boson and muonic puzzles.* 2016. **117**(10): p. 101801.

52. Deutsch, M. and S.C.J.P.R. Brown, *Zeeman effect and hyperfine splitting of positronium.* 1952. **85**(6): p. 1047.

53. Mills Jr, A. and G.J.P.R.L. Bearman, *New measurement of the positronium hyperfine interval.* 1975. **34**(5): p. 246.

54. Mills Jr, A., S. Berko, and K.J.P.R.L. Canter, *Fine-structure measurement in the first excited state of positronium.* 1975. **34**(25): p. 1541.

55. Ritter, M., et al., *Precision determination of the hyperfine-structure interval in the ground state of positronium. V.* 1984. **30**(3): p. 1331.

56. Hatamian, S., R. Conti, and A.J.P.r.l. Rich, *Measurements of the 2 3 S 1-2 3 P J (J= 0, 1, 2) fine-structure splittings in positronium.* 1987. **58**(18): p. 1833.

57. Conti, R., et al., *Search for C-violating, P-conserving interactions and observation of 23S1 to 21P1 transitions in positronium.* 1993. **177**(1): p. 43-48.

58. Hagena, D., et al., *Precise measurement of n= 2 positronium fine-structure intervals.* 1993. **71**(18): p. 2887.

59. Ishida, A., et al., *New precision measurement of hyperfine splitting of positronium.* 2014. **734**: p. 338-344.

60. Gurung, L., et al., *Observation of asymmetric line shapes in precision microwave spectroscopy of the positronium 2 S 1 3→ 2 P J 3 (J= 1, 2) fine-structure intervals.* 2021. **103**(4): p. 042805.

61. Steiger, T., et al., *Development of intense, long-lived positron sources.* Nuclear Instruments and Methods in Physics Research Section A: Accelerators, Spectrometers, Detectors and Associated Equipment, 1990. **299**(1-3): p. 255-260.

62. Khatri, R., et al., *Improvement of rare-gas solid moderators by using conical geometry.* 1990. **57**(22): p. 2374-2376.

63. Mills Jr, A.P. and E.J.A.P.L. Gullikson, *Solid neon moderator for producing slow positrons.* 1986. **49**(17): p. 1121-1123.

64. Danielson, J., et al., *Plasma and trap-based techniques for science with positrons.* 2015. **87**(1): p. 247.

65. Greaves, R., et al., *Positron trapping and the creation of high-quality trap-based positron beams.* 2002. **192**(1-2): p. 90-96.

66. Surko, C. and R.J.P.o.P. Greaves, *Emerging science and technology of antimatter plasmas and trap-based beams.* 2004. **11**(5): p. 2333-2348.

67. Surko, C.M., M. Leventhal, and A.J.P.R.L. Passner, *Positron plasma in the laboratory.* 1989. **62**(8): p. 901.

68. Murphy, T. and C.J.P.R.A. Surko, *Positron trapping in an electrostatic well by inelastic collisions with nitrogen molecules.* 1992. **46**(9): p. 5696.

69. Natisin, M., et al., *Positron cooling by vibrational and rotational excitation of molecular gases.* 2014. **47**(22): p. 225209.

70. Mills Jr, A., P. Platzman, and B.J.P.R.L. Brown, *Slow-positron emission from metal surfaces.* 1978. **41**(15): p. 1076.

71. Lynn, K.J.P.R.L., *Observation of surface traps and vacancy trapping with slow positrons.* 1979. **43**(5): p. 391.

72. Mills Jr, A. and L.J.P.R.L. Pfeiffer, *Desorption of surface positrons: A source of free positronium at thermal velocities.* 1979. **43**(26): p. 1961.

73. Mills Jr, A.P.J.S.S.C., *Thermal activation measurement of positron binding energies at surfaces.* 1979. **31**(9): p. 623-626.

74. Cassidy, D., et al., *Positronium formation via excitonlike states on Si and Ge surfaces.* 2011. **84**(19): p. 195312.

75. Canter, K., A. Mills Jr, and S.J.P.R.L. Berko, *Efficient positronium formation by slow positrons incident on solid targets.* 1974. **33**(1): p. 7.

76. Mills Jr, A.P.J.P.R.L., *Positronium formation at surfaces.* 1978. **41**(26): p. 1828.

77. Mills Jr, A., L. Pfeiffer, and P.J.P.r.l. Platzman, *Positronium velocity spectroscopy of the electronic density of states at a metal surface.* 1983. **51**(12): p. 1085.

78. Cassidy, D., et al., *Delayed emission of cold positronium from mesoporous materials.* 2010. **82**(5): p. 052511.

79. Day, D., et al., *On the formation of excited state positronium in vacuum by positron impact on untreated surfaces.* 2001. **34**(18): p. 3617.

80. Deller, A., et al., *Measurement of Rydberg positronium fluorescence lifetimes.* 2016. **93**(6): p. 062513.

81. Black, E.D., *An introduction to Pound–Drever–Hall laser frequency stabilization.* American journal of physics, 2001. **69**(1): p. 79-87.

82. Hood, C.J., H. Kimble, and J. Ye, *Characterization of high-finesse mirrors: Loss, phase shifts, and mode structure in an optical cavity.* Physical Review A, 2001. **64**(3): p. 033804.

83. Donley, E.A., et al., *Double-pass acousto-optic modulator system.* 2005. **76**(6): p. 063112.

84. Ley, R.J.A.s.s., *Atomic physics of positronium with intense slow positron beams.* 2002. **194**(1-4): p. 301-306.

85. Bruvelis, M., et al., *Analytical model of transit time broadening for two-photon excitation in a three-level ladder and its experimental validation.* Physical Review A, 2012. **86**(1): p. 012501.